Relationship of magmatic fluids to high-enthalpy geothermal systems: New insights from the Tolhuaca Geothermal System (TGS), Southern Andes

Philippe Robidoux, Daniele Tardani, Pablo Sánchez-Alfaro, Marco Liuzzo, Diego Morata, Yves Moussallam, Estelle Rose-Koga, Franco Tassi, Pamela Pérez-Flores, Fausto Grassa, et al.

Journal of Geochemical Exploration

«Relationship of magmatic fluids to high-enthalpy geothermal systems: new insights from the Tolhuaca Geothermal System (TGS), Southern Andes»

--Manuscript Draft--

Manuscript Number:	
Article Type:	Research Paper
Keywords:	Geothermal system; Tolhuaca volcano; Igneous geothermobarometry; Inclusions; Gas geochemistry
Corresponding Author:	Philippe Robidoux Department of Geology and Andean Geothermal Center of Excellence (CEGA), Universidad de Chile Santiago, Chile
First Author:	Philippe Robidoux
Order of Authors:	Philippe Robidoux
	Daniele Tardani, PhD
	Pablo Sanchez-Alfaro, PhD
	Yves Moussallam, PhD
	Estelle Rose-Koga, PhD
	Marco Liuzzo
	Diego Morata, PhD
	Franco Tassi, PhD
	Pamela Pérez-Flores, PhD
	Fausto Grassa
	Vincenzo Francofonte
Abstract:	Highlights • Magma gas supply to the Tolhuaca Geothermal System since post-glacial period • Volatile melt separation zone at 0.9–1.1 km, just below water boiling depth • CO2-H2S equilibrium of melt-volatile mix modified below geothermal vapor zone • Tolhuaca magma records polybaric crystal fractionation from 2–50 km • MORB-like noble gas signature imprints magma as does geothermal fluid chemistry
Suggested Reviewers:	Samuel Scott, Dr. PostDoc Researcher, University of Iceland samuel.scott@erdw.ethz.ch Dr. Scott researches involve high enthalpy geothermal systems and magmatism. The geological background and knowledge of these fields will help to give a resourcefull review. Alternative email is "samuels@ru.is".
	Marine Collignon, Dra PostDoc Researcher, University of Geneva marinec1709@gmail.com Dra Collignon have field experience working on Tolhuaca and rich geological view of the geothermal system. The works on surface CO2 mapping made by the researcher revealed important key aspects on surface degassing.

Cover Letter

Santiago, June 16, 2023

Journal of Geochemical Exploration of Editorial Board
Section Editor-in-Chief
Prof. Stefano Albanese

Dear Editor,

On behalf of the co-authors, I submitting the manuscript by Robidoux et al. entitled **«Relationship of magmatic fluids to high-enthalpy geothermal systems: new insights from the Tolhuaca Geothermal System (TGS), Southern Andes»** for consideration in Journal of Geochemical Exploration, as Research Article**.**

We report here on the evidence from petrogenesis, magma and gas chemistry to confirm a typical high-enthalpy geothermal system like Tolhuaca Geothermal System (TGS) is connected to a magmatic intrusive body through the circulation of magmatic fluids from mantle to surface. We present the first measurements noble gas (He-Ne-Ar) isotopic compositions of fluid inclusions trapped in olivines from Holocene to post glacial volcanic rock of Tolhuaca volcano (≤17 kyr), belonging to the Southern Volcanic Zone (SVZ) of the Andes. Within this study, we constrain a magmatic 3He/4He signature of 8.2 Ra, within the MORB range (8±1 Ra) and confirm the mantle signature of surface gas source. Based on bulk rock chemistry from Minor eruptive vents on Tolhuaca flanks, parental magmas are generated by incorporation of slab-rich fluids with low sediment input evidenced by our new collection of rare earth and trace elements from bulk rock analyses. Our petrological data are put in the context of pressure and temperature conditions (~< 1163 °C, ~< 60 km equivalent crustal depth) of syn glacial to post glacial magmatic events as estimated with Mineral liquid geothermobarometers. The first melt inclusion volatile solubility models are also presented at Tolhuaca volcano, here showing that the volatile melt separation zone is located at 0.9–1.1 km, just below water boiling depth (0.95 km) reported from exploration wells in literature. The CO_2-H_2S relative equilibrium contents of melt-volatile is changing at 1.8 km below surface, in near coincidence with deepest hydrothermal reservoir also reported by geophysical methods to track geothermal as magma sources below Tolhuaca.

Despite magma may not show evidence of historical to present surface eruptions and ascents as neighbor active volcanic systems (Lonquimay, Copahue, Llaima), Tolhuaca magmatic vapor still feed the surface degassing system. The major gas species of surface fumaroles is measured here with MultiGAS and supported with direct sampling using the Giggenbach method, altogether show atmospheric contamination (low CO_2/Ar) but higher CO_2/H_2S and CO_2/CH_4 ratios relative to fumaroles on the lower Tolhuaca flanks, which may be caused by the scrubbing effects on H_2S within a hydrothermal reservoir (~1.5 km) close to the heat source and upflow geothermal zone. The definition of such geochemical features and saturation pressure of magma vapor zone with melt inclusion volatile models help to estimate the depth location of the thin layer that separates roof of magma bodies from the high-enthalpy geothermal systems, therefore representing powerful tools for geothermal exploration.

This work and the data presented are original and were never published elsewhere. I look forward to hearing from you. Best regards,

Philippe Robidoux

robidouxphilippe@gmail.com

Via Ersilia 803, Santiago, Chile – Tel. +56951232150 –
e-mail: philippe.robidoux@uchile.cl

Highlights

- Magma gas supply to the Tolhuaca Geothermal System since post-glacial period
- Volatile melt separation zone at 0.9–1.1 km, just below water boiling depth
- CO_2-H_2S equilibrium of melt-volatile mix modified below geothermal vapor zone
- Tolhuaca magma records polybaric crystal fractionation from 2–50 km
- MORB-like noble gas signature imprints magma as does geothermal fluid chemistry

Title: «Relationship of magmatic fluids to high-enthalpy geothermal systems: new insights from the Tolhuaca Geothermal System (TGS), Southern Andes»

Author names and affiliations. Philippe Robidoux[a,b]; Daniele Tardani[b,c], Pablo Sánchez-Alfaro[b,d], Marco Liuzzo[e,f], Diego Morata[a,b], Yves Moussallam[g,h], Estelle F. Rose-Koga[i], Franco Tassi[j], Pamela Pérez-Flores[k], Fausto Grassa[e], Vincenzo Francofonte[e]

[a] Department of Geology, Facultad de Ciencias Físicas y Matemáticas, Universidad de Chile, 8370450 Santiago, Chile

[b]Andean Geothermal Centre of Excellence (CEGA), University of Chile, Santiago, Chile

[c]University of O'Higgins, Institute of Engineering Sciences, Rancagua, Chile

[d]Instituto de Ciencias de la Tierra, Universidad Austral de Chile, Valdivia, Chile

[e]Istituto Nazionale di Geofsica e Vulcanologia, Sezione di Palermo, Via Ugo La Malfa 153, 90146, Palermo, Italy

[f]Università di Ferrara - Polo Scientifico Tecnologico, Dipartimento di Fisica e Scienze della Terra, Via Giuseppe Saragat, 1 44122 Ferrara , Italy

[g]Lamont-Doherty Earth Observatory, Columbia University, New York, USA

[h]American Museum of Natural History, Department of Earth and Planetary Sciences, NY 10024, New York, USA

[i]Institut des Sciences de la Terre d'Orléans, 1A Rue de la Férollerie, Orléans Cedex 2, France

[j]University of Florence, Department of Earth Sciences, Firenze, Italy

[k]Consultoria e Investigación Geológico Ambiental Ltda, Huasco, Chile

Corresponding author.

Dr. Philippe Robidoux

Department of Geology, Facultad de Ciencias Físicas y Matemáticas, Universidad de Chile, Plaza Ercilla 803, 8370450 Santiago, Chile

E-mail address: robidouxphilippe@gmail.com (P. Robidoux)

Keywords

Geothermal system, Tolhuaca volcano, Igneous geothermobarometry, Inclusions, Gas geochemistry

Highlights

- Magma gas supply to the Tolhuaca Geothermal System since post-glacial period
- Volatile melt separation zone at 0.9–1.1 km, just below water boiling depth
- CO_2-H_2S equilibrium of melt-volatile mix modified below geothermal vapor zone
- Tolhuaca magma records polybaric crystal fractionation from 2–50 km
- MORB-like noble gas signature imprints magma as does geothermal fluid chemistry

ABSTRACT

The Tolhuaca Geothermal System (TGS) represents a potential 13 Mwe geothermal reservoir located on the NW flank of Tolhuaca stratovolcano, in the Southern Volcanic Zone (SVZ) of the Andes. Despite decades of scientific exploration into the surface hydrothermal chemistry, its definition as a high-enthalpy geothermal system and its connection to the underlying magmatic system had not previously been demonstrated. A novel combined approach using Multigas-Giggenbach gas monitoring has found that the TGS magma-gas component is dominated by CO_2-rich fluids (relatively high CO_2/H_2S and CO_2/CH_4) that feed the fumaroles and exploration wells in the Amphitheater structure. Gas measurements near the summit of Tolhuaca show little atmospheric contamination (low CO_2/Ar) but higher CO_2/H_2S ratios relative to fumaroles on the lower flanks (Pablo Sola field), which may be caused by the scrubbing effects on H_2S within a hydrothermal reservoir at less than ~1.5 km beneath the surface (permeable geothermal zone). The atmosphere-corrected $^3He/^4He$ ratio (Rc/Ra) measured by bulk fluid inclusion (FI) analysis of olivines from the Cono Canción minor eruptive center (6.40±0.38 Ra) is similar to other fumarole systems measured in the literature that are <400 m from the vent (6.49±0.05 Ra). The magma erupted from this center is andesitic to dacitic in composition; it is cool (T ~< 980 °C) and oxidized (NNO = 2.0–3.0), with evidence of crustal contamination. There are two stages of crystallization and magma mixing, identified using mineral-liquid geothermobarometers (<50-60 to <14 km). In addition, minor amounts of crustal-derived ^4He indicate alteration of the initial ^3He-rich magmatic fluids ($1.37 \cdot 10^{-9}$ $CO_2/^3He$). In contrast, melt inclusions from olivines in the syn-glacial Tolhuaca Fissural MEC give values of 8.16±0.63 Ra in (typical SVZ regional MORB signature), indicating a single <31 km magma ascent episode of hot (~< 1163 °C) weakly oxidized (NNO = 0.5–1.5) basaltic to basaltic andesite melt which has preserved the magmatic ^3He in fluid

inclusions ($2.64 \cdot 10^{-8}$ $CO_2/^3He$). Based on bulk rock chemistry from Cono Caracol, Coli and Tolhuaca Fissural eruptive centers, parental magmas are generated by incorporation of slab-rich fluids (high Ba/La) with low sediment input (low U/Th). For the first time in this region, we use melt inclusions (MI) to investigate the magma-volatile component of a magmatic plumbing system in the context of geothermal exploration (parental melts contain 1.94 wt% H_2O, 2496 µg/g CO_2, 142 µg/g S, and 1095 µg/g Cl). The volatile dataset from the melt inclusions agrees with decompression and degassing models, interpreted here as resulting from magmatic release of water and oxidized sulfur at depths of 1.08–1.8 km, inferred to be the primitive vapor feeding the geothermal vapor zone. This is a few tens of meters below the water boiling point identified in past exploration well studies at TGS (0.95 km). This new solubility model provides a means of combining geothermal exploration with location of magma depth, and of geochemically characterizing the narrow vertical window between the base of characteristic hydrothermal convection cells and the roof of the underlying magmatic system in other high enthalpy geothermal systems around the world.

1. Introduction

There are a number of high enthalpy geothermal systems in southern Chile (Lahsen et al., 2005), characterized by high ground temperatures at shallow depths close to active volcanic systems (Stober and Bucher, 2021). They provide potential sources of green energy for the human settlements near to the volcanic center (Quick et al., 2013; Daniele et al., 2020). Of the known sites in Chile (e.g., Cerro Pabellón, El Tatio, Tolhuaca; Aravena et al., 2016), the Tolhuaca Geothermal System (TGS) has undergone decades of geothermal exploration (Sánchez-Alfaro et al., 2015; Vargas Payera et al., 2022), which provides background material for further scientific investigation into the depth and origin of the TGS epithermal fluids (Melosh et al., 2012; Sánchez-Alfaro et al., 2016).

Tolhuaca volcano (summit 2,739 m: 38°18′36″S 71°38′42″W) is located in the Southern Volcanic Zone (SVZ) of the Chilean Andes, 40 km east of the town of Curacautín and 170 km to the west of the Argentinian border (Fig. 1a). The TGS (Fig. 1bc) is an excellent potential source of energy production, with a value of 13 Mwe measured at wellheads (Aravena et al., 2016). The geothermal reservoir of ~300°C is likely located at a depth of 1.5 km based on temperature logging, while direct sampling of fluid chemistry, temperatures from fluid inclusions (FI) and present-day residual waters from Tol-1 well indicate fluid mixing and boiling down to a depth of ~1 km, at which depth metal-rich fluids are known to circulate crossing a propylitic alteration zone (e.g. Moore, 2009; Sánchez-Alfaro et al., 2016; Tardani et al., 2017). There are no existing studies on the igneous processes and P-T magmatic fluid conditions below the geothermal zone at Tolhuaca, so this study is designed to determine the chemical fluid signature of the localized geothermal reservoir and to connect it to the magmatic system within the broader framework of geothermal exploration in volcanic arcs.

The aim is to determine if the geothermal gases are sourced from the same plumbing systems in which melt inclusions (MI) and fluid inclusions (FI) have been

trapped, using the regional minor eruptive centers (MEC) that constitute the current Tolhuaca composite volcanic structure (Thiele et al., 1987). The major gas components (H_2O-CO_2, S) were determined by portable MultiGAS instruments (INGV laboratories, Italy) across the TGS (Pablo Sola: PS; Jaime Muro: JM) to monitor spatial changes in measurements of fumarole gases, together with direct gas measurements at fumaroles and borehole sites (Tol-1, 2, 3) (Sano and Fisher, 2013). Pre-eruptive magma compositions from MEC were determined in MI by electron microprobe analysis (EMPA) and volatile contents (H_2O-CO_2, S, Cl, F) using secondary ion mass spectrometry (SIMS) (Wallace et al., 2021). The chemistry of magmatic fluids coming from deeper plumbing channels was investigated using the noble gases preserved in FI in olivine crystals ($^3He/^4He$, $^{40}Ar/^{36}Ar$, $^{20}Ne/^{21}Ne/^{22}Ne$) (e.g. Copahue; Roulleau et al., 2018). The results have been used to create a geochemical model to explain post-glacial to present-day magmatic fluid transport conditions at Tolhuaca, which can be used as a model for linking individual high enthalpy geothermal fields to their related volcanic system.

2. Geological background

2.1 Context for magma-fluid transport in the Southern Andes

The Southern Volcanic Zone (SVZ) is bounded by the Juan Fernandez Ridge to the north (~33°S) and the Chile Rise to the south (~46°S) (Fig. 1a). Volcanism in the Andes is the result of the subduction of the Nazca and Antarctic oceanic plates (over the last 45 Myr) beneath the South American continental plate (Stern, 2004), advancing obliquely (20–30°) towards the NE at a rate of 7–9 cm/yr (DeMets et al., 2001). The crustal basement beneath the Pleistocene-Holocene SVZ stratovolcanoes is ~ 35–60 km thick above a shallowly dipping (< 25°) Benioff zone (Tassara and Echaurren, 2012). Here the mantle wedge is less thick (~ 50 km), and the overlying crust is much younger, composed of Paleozoic pre-Andean basement and Mesozoic-Cenozoic igneous rocks (Stern, 2004).

In the southern segment of the SVZ (34–39°S), the Liquine-Ofqui Fault System (LOFS; Cembrano et al. 2000) determines the location of many of both the larger and smaller volcanic eruptive centers (McGee et al., 2019). The stratovolcanoes and calderas in the southern part of the SVZ are largely controlled by NW-SE and NE-SW faults (e.g. Tolhuaca, Fig. 1b). The complex interaction between tectono-magmatic and hydrothermal processes is shown by both the structure and geochemical signature of the volcanic-hydrothermal systems in the Central to Southern VZ (Hilton, 1993; Cembrano & Lara, 2009; Tardani et al., 2016; Wrage et al., 2017). Two endmember volcano–tectonic-hydrothermal associations have been identified (Lopez-Escobar et al., 1995) with (1) NE-striking volcanic alignments (< 58 %wt SiO_2 lithologies) of either stratovolcanoes or minor eruptive centers (Cembrano and Lara, 2009), and (2) WNW-striking alignments of stratovolcanoes with a more evolved magma series (basaltic to rhyolitic). NW-trending

volcanoes are potentially related to the presence of the Andean Transverse Fault (ATF) system (Fig. 1b).

The stratovolcanoes and MECs in the Central Volcanic Zone (CVZ) and the SVZ produce tholeiitic and high-Al basalt and basaltic andesites. Eruptive products are mainly of basaltic to andesitic composition (50–58% SiO_2), with a predominance of products of basaltic-andesite composition (52–56% SiO_2) (Hickey-Vargas, 2002). Magmatic fluids are characterized by MORB-like helium isotope ratios initially observed in northern (CVZ) and southern Chile (SVZ; 8.0 and 7.9 RA, respectively; Fig. 1a), where the crust is 45–30 km thick. Both have high sedimentary flux margins, and according to Lages et al. (2021) this reflects a more efficient delivery of radiogenic He into the wedge from the subducted (U-Th-rich) terrigenous sediments (Kagoshima et al., 2015).

2.2 Geology of Tolhuaca volcano and geothermal system characteristics

Tolhuaca stratovolcano, popularly referred to as "*Tolwaca*" by local Mapuches communities, is located ~270 km from the volcanic arc trench (Fig. 1a) at which point the continental crustal thickness reaches 35 km and subduction angle is 25° (López-Escobar et al., 1995). The volcano is located at the intersection of the two major structural elements, the LOFS and ATF lineaments (Pérez-Flores et al., 2012, 2017b), and these two fault systems represent pathways for ascending magma and fluids (Pérez-Flores et al., 2014, 2017b; Sánchez-Alfaro et al., 2016; Fig. 1b). Tolhuaca rises ca. 900 m above its basement and is composed of both lava and pyroclastic flows (detailed in Fig. 1b, Pérez-Flores et al., 2017). According to studies in Suárez y Emparán (1997), the volcano is built on the Cura-Mallín Formation (Oligocene-Miocene, ca. 8–22 Myr) which forms the basement, which is composed of andesite to rhyolite volcanic rocks interbedded with sedimentary rocks. This formation is followed by the Malleco Formation (Pliocene-Lower Pleistocene; ca. 1–4 Myr), a volcanic complex built from volcanic as well as continental sedimentary facies. Both geological formations are cross-cut by Miocene granitic rocks of the Patagonian Batholith.

The Tolhuaca volcanic units are synchronous with the Quaternary stratovolcanoes at the present volcanic arc front (Lonquimay, Llaima, etc.). The lava and pyroclastic flows of basaltic and basaltic-andesite compositions are mainly calc-alkaline (Moreno et al., 2012). The mafic end members from the Tolhuaca volcanic system are interbedded with andesite and dacite lava flows (Lohmar et al., 2012; Melosh et al., 2012) which date back to at least ca. 290 ka (Ar-Ar method, Polanco et al., 2014). Volcanism also occurred at 160 ± 30 ka, with NW-striking fissure activity on the NW flank and again at 60 ± 30 ka (Ar-Ar method, Polanco et al., 2014). Tolhuaca is spatially and genetically associated with the LOFS, which is a transpressional tectonic regime (predominantly dextral strike-slip deformation interpreted from shallow seismic activity (<25 km depth) (Lange et al., 2008; Legrand et al., 2011). One major NW-striking fault appears to be the source of most of the hydrothermal fluids (Sánchez-Alfaro et al., 2016) (Fig. 1c). The conjugate system of the ATF includes a series of NW-striking structural lineations of pre-Andean origin (Radic,

2010) with sinistral reverse kinematics and local re-activation of normal faults (Cembrano and Lara, 2009; Sánchez-Alfaro et al., 2016; Pérez-Flores et al., 2016). The NW fissure also records volcanic activity from after the last glacial retreat (<17.8 kyr BP) (Moreno et al., 2012, 2015).

Post-glacial lava flows and pyroclastic deposits of ~<6 kyr old have been identified on the NW flank of Tolhuaca as the “Pemehue Volcanic Trend” (Moreno and Gardeweg, 1989; Polanco et al., 2000). This is assumed to refer to the Upper-Late Pleistocene volcanic units (Moreno, H. et al. en prep.) named Cono Canción (post-glacial) and Tolhuaca Fissural (syn-to-post glacial) (Gatica, 2022) shown in maps from Stimac (2012, unpublished). All these beds are shown on the maps of Thiele et al. (1987) (Fig. 1c). Other Holocene MEC, Cono Caracol and Cono Coli, follow a NE-SW direction (Thiele et al., 1987; Moreno, H. et al. en prep.) (Fig. 1c). Two episodes of explosivity or presence of a crater plume have been mentioned during the 19-20th century (Melosh et al., 2012), but there is no official record of historical eruptions at Tolhuaca volcano. Volcanic rock products linked to the 8.05–6.59 kyr BP activity are the only confirmed evidence of explosive activity at the summit crater (Thiele et al., 1987; Suarez and Emparan, 1997; Polanco, 2000; Lohmar et al., 2012).

During the exploration phase at the Tolhuaca geothermal field from 2009-2016 (Vargas Payera et al., 2022), the drill core was used to establish a detailed log of the geological units (Tol-1, 2, 3, 4; Fig. 1c) (Stimac, 2012, unpublished). Rock units in drill core Tol-1 revealed mainly lavas, in-situ breccias, volcanoclastics and minor tuffs, hyaloclastites, and pillow breccias down to the Cura-Mallín Formation at a depth of 500 m (Melosh et al., 2010, 2012; Lohmar et al., 2012; Sánchez-Alfaro et al., 2016). Based on secondary minerals from the drill core samples, three main facies-related alteration zones were detected: (1) an upper zone of argillic alteration (<20–450 m), estimated at 300 m according to magnetotelluric (MT) study (Pavez et al., 2022); (2) an intermediate zone with sub-propylitic alteration (450–650 m); and (3) a deeper zone of propylitic alteration (>650 m) (Melosh et al., 2010, 2012; Sánchez-Alfaro et al. et al., 2016; Tardani et al., 2017).

Geochemical studies of the major gas species suggest the existence of a geothermal reservoir in the NW of the area at a depth of ~1.5 km (1.8 km for deep limit of reservoir by MT in Pavez et al., 2022) with an estimated temperature of 220–300 °C, overlain by an aquifer at ~160 °C (Melosh et al., 2010, 2012). Most of the hot springs and fumaroles lie along the NW-trending fissures mapped by Hauser (1997) and Melosh et al. (2010, 2012, and references therein). This series of high-sulfur springs and fumaroles defines the so-called Tolhuaca Geothermal System (TGS; Melosh et al., 2010). The borehole heads Tol-1 to Tol-4 at the discharge gas site FM occur inside a collapsed area SE of the TGS sector (Fig. 1c), which borehole studies show to be bounded by a normal fault and a reverse fault (Melosh et al., 2012; Stimac, 2012). The horseshoe structure of this collapse area could be related to glacial erosion and/or volcanic activity (Collignon et al., 2021). The hydrothermal sector covers an area of ca. 300 m^2, encompassing the main concentration of fumaroles with sulfur and secondary salt accumulations (Melosh et al., 2012). It should be noted that the degassing structures grade into other thermal sites down the NW Tolhuaca flank (PS and Ganado Afanado thermal sites) (Collignon et al.,

2021), reaching as far as the regional sinistral Adobe fault (Pérez-Flores et al., 2017; Arroyo Alarcón, 2018) (Fig. 1c). Here conjugate sinistral-reverse faults and crush zones crosscut the Cura-Mallín Formation whose high topography acts as a barrier to most of the Tolhuaca Fissural and Cono Canción lavas.

Initial direct sampling was performed exclusively in the geothermal exploration sites (JM in Fig. 1c), for example Melosh et al. (2010, 2012), and indicated a range of CO_2 content (79.3–93.2%), and a broad range of CO_2/S ratios from 7.2–170.9. The total average CO_2 release of the most important discharge sites is given by Collignon et al. (2021) from gas mapping (Chiodini et al., 1998 method) carried out in 2020 using an accumulation chamber at the PS (~3.13 T/d) and JM sites (~0.77 T/d). The JM site was also sampled in January 2014, giving a recorded temperature of 92 °C, and its fumarole contained mainly H_2S (1.10%) and CO_2 (95.2%), with helium isotopes of 6.49 +/- 0.05 (Rc/Ra) (Tardani et al., 2016).

3. Methods

3.1 Automatic in-situ field gas mapping

Gas samples were measured for their H_2O, CO_2 and H_2S compositions at the geothermal fields from November-December 2021 using a portable multicomponent gas analyzer system capable of sampling at 1 Hz (Aiuppa et al., 2006; Shinohara, 2005). The MultiGAS instrument was used on different types of discharge site; fumaroles, bubbling hot springs, hot mud pools, and thermal water springs (Table S1). The sensor assemblage used in this study is described in Gurrieri et al., (2021) and Boudoire et al. (2022). Data were processed using the Ratiocalc software to calculate molar ratios between individual volatiles (Tamburello, 2015). The TGS gas sampling was designed to cover key hydrothermal discharge sites on the NW Tolhuaca flank; 1) at high altitude and close to the youngest MEC (Cono Canción), which corresponds to the JM field, and 2) at lower altitudes, corresponding to the PS sector. The temperature (T), pressure (P) and relative humidity sensors (Rh) were recorded to estimate water concentration using the Arden-Buck equation (Buck, 1981).

3.2 Direct *in situ* fumarole and borehole gas sampling

To maximise identification and quantification of the fumarole gas, direct gas sampling was carried out at the PS fumaroles (PB1, 2, 3; Table 2) to complement previous analyses at the JM fumarole site using a pre-evacuated 150 mL glass flask filled with 75 mL of a 4N NaOH solution (Tardani et al., 2016). The bubbling gas from hot springs was sampled in double valve, pre-evacuated alkaline glass containers, using pure silicone tubes connected to an inverted funnel and a manual pump (Sano and Fischer, 2013).

Giggenbach bottles were used to store gas samples collected from the fumaroles using a titanium tube which was inserted into the fumarole, vent or well boreholes. Well sampling, focusing on wells Tol-1, 2, and 3, was carried out in 2014 when the private company undertaking the geothermal field exploration granted access to researchers (Fig. 1c). The gases stored in the soda flask headspace (N_2, $Ar+O_2$, H_2, He, and CO) were analyzed at the Laboratory of Fluid and Rock Geochemistry (Florence, Italy) using gas-chromatography Shimadzu GC-15° with Thermo Focus GC. A methanizer coupled to a Gas Chromatographer Flame Ionization Detector (GC-FID) enabled the detection of very low concentrations of carbon monoxide (CO) and methane (CH_4). Hydrogen sulphide (H_2S) concentrations were determined by analysing sulphate in the soda solution by ion-chromatography after oxidation with H_2O_2, while acidimetric titration with 0.1N HCl was used to analyze CO_2 dissolved in the soda solution as CO_3^{2-} (Tassi et al., 2010). Analytical errors were <5% for the main gas components and <10% for minor and trace gas compounds (Tassi et al., 2010).

3.3 Petrography and mineral inclusion selection

To obtain the best-preserved mineral inclusions (MI), we systematically sampled known volcanic deposits for juvenile pyroclasts at the following four volcanic centers (in inverse chronological order): Cono Canción (CC), Cono Caracol, Cono Coli and Tolhuaca Fissural (TF) (Fig. 1c). Olivine, pyroxene and plagioclase crystals were separated from the 0.5 to 2 mm fractions of the original ash and crushed scoria layers using a heavy liquid (sodium polytungstate), then by magnetic separation and finally careful handpicking under a binocular microscope at Universidad Mayor (Santiago, Chile). Selected crystals were cleaned using the Di Piazza et al. (2015) protocol to accumulate the maximum mass of mafic crystals. Homogeneous glassy crystal-hosted MI (Cannatelli et al., 2016) were carefully selected and single crystals polished individually using silicon carbide mats for coarse polishing and aluminum oxide for the final stages at 6 µm, 3 µm, 1 µm and 0.1 µm. Details of the analytical methods are given in Rose-Koga et al. (2021).

Mineral identification and quantification in thin section was performed using a scanning electron microscope (SEM) FEI Quanta 250, at the Department of Geology, Faculty of Physical and Mathematical Sciences, University of Chile. Analytical conditions were 20 kV accelerating voltage, a vacuum pressure of 10^{-4} Pa, 85 µA emission current and electron beam emitter at 10^{-11} µm for all measuring points.

3.4 Whole rock major and trace element analyses

To investigate the petrogenetic processes by means of geochemical results, bulk rock from n = 12 volcanic fragments were analyzed by X-Ray Fluorescence (XRF) and Inductively Coupled Plasma-Mass Spectrometry (ICP-MS). ICPMS analyses were obtained to determine major element whole rock compositions of samples collected. Powders were prepared using the rock crusher at U. Mayor, Escuela de Geología (Santiago, Chile), and sent to a private laboratory for analysis (ActLabs, Canada). The samples were analysed for trace elements, specifically transition metals (Ni, Cr, Zr and V), large ion lithophile elements (Sr, Rb, Ba, Th and U), high field strength elements (Hf, Ta) and rare earth elements (the lanthanides La to Lu).

3.5 Major elements in mineral and glass inclusions

Electron microprobe analysis (EMPA) was used to determine the major element content in mineral-glass rim pair samples, and also for the glass inclusions they hosted. Inclusions, interstitial glass, and mineral chemistry were probed with an electron microprobe analyzer (EMPA), model JXA-8200 (JEOL), equipped with five wavelength-dispersive X-ray spectrometers and one energy-dispersive X-ray spectrometer analyzer, at the HPHT (high-pressure/high-temperature) laboratory of the Istituto Nazionale di Geofisica e Vulcanologia (INGV) in Rome (Italy). Polished phenocrysts were placed on indium mounts and were probed by EMPA, including any inclusions present in the phenocrysts, before being pressed for 24 hrs. The EMPA conditions were a beam current of 7.50 nA, accelerating voltage of 15 kV, and beam diameter of 5 μm. The counting times for the minerals were 10 and 5 s at the peak and background, respectively. In Table S2, mineral standards from INGV (Rome) are shown for augite “aug7552” and olivine “Ol” in addition to the U.S. National Museum glass standard (Hauri et al., 2002) including fragments of basaltic glass “ALV519-4-1” and basaltic andesite glass “GL07 D30-1”; all of which were probed for duplicate spots to verify reproducibility of results from major elements (0.08–0.19 S.D.%). The set of reference X-ray Crystals in the wavelength-dispersive channels are detailed in Table S2.

The compositions of MI in olivines were corrected for post-entrapment crystallization (PEC) and for Fe-loss using Petrolog3 code (Danyushevsky and Plechov, 2011). An equilibrium Fe-Mg distribution coefficient between olivine and liquid (Kd Fe-$Mg_{ol\text{-}liq}$) of 0.30 was applied (Toplis, 2005), incrementally adding the olivine composition to the MI until the equilibrium Kd value (0.30) with the host olivine was reached. The melt $Fe^{3+}/\sum Fe$ ratio was determined using the measured bulk rock composition Fe^{2+}/Fe^{3+} ratio from the titration method. The Ni–NiO buffer (NNO) (Kress and Carmichael, 1991), commonly considered the most realistic fO_2 for arc magmas (e.g. Jugo, 2009), was used with the Putirka et al. (2008) Olivine-L geothermometer to estimate temperature entrapment conditions up to complete PEC. Similarly, melt inclusions hosted in

clinopyroxene phenocrysts were corrected for PEC with an Excel custom-made spreadsheet, adding clinopyroxene increments to the melt inclusions until the equilibrium Kd Fe-$Mg_{cpx\text{-}liq}$ = 0.26, was reached, at an fO_2 = Ni-NiO.

3.6 Secondary Ion Mass Spectrometry (SIMS) on glass inclusions

The volatile (H_2O, CO_2, Cl, F, S) concentration in melt inclusions, embayments, and matrix glasses was determined using a Cameca IMS 1280 ion microprobe at CRPG-CNRS-Nancy (France). A Cs^+ primary beam was used with a current of 1 nA and an electron gun to compensate for charge build-up at the sample surface. A 3-minute pre-sputter with a 30 × 30 µm square raster was applied, then analyses were performed on the 15 to 20 µm spot in the center of the rastered-clean area by a mechanical aperture placed in the secondary ion image plane. The mass resolving power of ≈7000 (corresponding to a contrast aperture at 400 µm, the energy aperture at 40 eV, the entrance slit at 52 µm and the exit slit at 173 µm) made possible the complete discrimination of mass interferences ($^{34}S^1H$ on ^{35}Cl, ^{17}O on $^{16}O^1H$, $^{29}Si^1H$ on ^{30}Si and $^{31}P^1H$ on ^{32}S). We collected signals for ^{12}C (8 seconds), ^{17}O (3 seconds), $^{16}O^1H$ (6 seconds), ^{18}O (3 seconds), ^{19}F (4 seconds), ^{27}Al (3 seconds), ^{30}Si (3 seconds), ^{32}S (4 seconds) and ^{35}Cl (6 seconds; counting times in parenthesis), with 2 seconds waiting time after each switch of the magnet. This cycle was repeated 10 times for each analysis. One measurement lasted 12 min per spot.

The concentrations were determined using calibration curves (Fig. S1) obtained at the beginning, middle, and end of each session, by measuring a set of natural basaltic glasses under the same analytical conditions (KL2G, Jochum et al. 2006; KE12, Mosbah et al. 1991; VG2, Jarosewich et al. 1980; experimental glasses N72, M35, M40 and M48, Shishkina et al. 2010 and MacQuarie glasses 47963 and 25603, Kamenetsky et al. 2000) with a large range of concentrations of volatile elements overlapping those of our samples. Maximum errors, based on reproducibility over 10 cycles of analysis, were less than 15% for CO_2, 3% for Cl, 4% for S, and 5% for F and H_2O (Fig. S1). A total of n = 11 glassy melt inclusions, without shrinkage bubbles nor PEC artefacts were measured.

3.7 Noble gases from mafic phenocrysts

The noble gas signature provides insight into the origin of trapped magmatic fluids (gas and liquids), with here a total n = 5 sets of homogeneous olivine crystals with fluid inclusions (FI) from Tolhuaca. Those fluids preserve a sufficient concentration ($1•10^{-16}$ - $1•10^{-11}$ mol/g) of noble gases (helium, neon, argon) to be analysed for their relative isotopic ratios ($^3He/^4He$, $^{40}Ar/^{36}Ar$, $^{20}Ne/^{21}Ne/^{22}Ne$). Laboratory measurements were performed at INGV-Palermo (Italy) (following protocols from Rizzo et al., 2016 and

references therein). Noble gases trapped in FI are released by in-vacuo single-step crushing, then extracted on release from the mechanical fragmentation of crystals which are cleaned in an ultra-high-vacuum purification line. A multicollector mass spectrometer (GVI Argus) was used to measure Ar isotopes (^{36}Ar, ^{38}Ar, and ^{40}Ar). A Helix SFT-Thermo instrument was used to measure helium and neon isotopes separately using a split flight tube mass spectrometer. The $^{3}He/^{4}He$ ratios are given in units of R/Ra (where Ra is the $^{3}He/^{4}He$ of air; i.e., 1.39×10^{-6}). The R/Ra values require correction for atmospheric contamination based on $^{4}He/^{20}Ne$ (e.g. Sano and Wakita, 1985) and are expressed as Rc/Ra in the final values.

4. Results

4.1 Chemical composition of gases

The chemical composition of hydrothermal field gases at discharge sites are reported in Table 1 (details in Table S1) and full results of total gas compositions at fumaroles and wells are shown in Table 2. The Multigas data from the JM and PS sites are presented consecutively with altitude-dependent internal pressure being 787–792 bars at JM and 822–824 bars at PS (Table S1). The gas composition is dominated by CO_2 (833 [ppmv] average) with moderate H_2S concentrations (2.3 [ppmv] average). The sulfur species at both JM and PS were dominated by H_2S (Fig. 2, 3ab), which has thus been used to represent the total derived sulfur content (hereafter S_t). This is consistent with thermal conditions which do not meet typical high-temperature plume-fumarole conditions (450°C: Symond et al., 2001; Fisher and Chiodini, 2015). It is therefore assumed that the main gas species present in the geothermal system are H_2O, CO_2, CH_4 and H_2S (for discussion of methane see figure 3b). At both places, the CO_2 threshold concentration varies between 470–1159 (ppmv), with a maximum peak value of 1292 (ppmv). The threshold concentration of H_2S varies from 1.1–6.4 (ppmv), with a peak value of 9.3 (ppmv). The Arden-Buck equation using Rh, T and P was used to estimate the water concentration (interval ~13,030–32,300 [ppmv]) relating to the intervals of measured Rh (40–74.6%).

The fumaroles observed in the JM sector show a larger range of CO_2/S_t ratios, of between 58.3–178 (FM8 had a value of 232, but appeared to be completely dry). The PS sector has a denser emission of steam which is characterized by a CO_2/S_t ratio of between 19.2–88.1. The H_2O/CO_2 ratio at JM ranges from 3.14–1.8 (R^2>0.87; range for err. 1σ = 1.7–5.4), while at PS it ranges from 1.2–4.81 (R^2>0.84; range for err. 1σ = 0.53–4.5) (except outliers 481, 7737; Table S1). The H_2O/H_2S is 436 at JM (R^2=0.91; err. 1σ = 254), while at PS the full range is 100–1503 (R^2>0.78; range for error 1σ = 75–897). The ternary plot (Fig. 2) confirms that the group of discharging sites found closer to the CO_2-rich endmember corresponds to the dry fumarole type. Sampled sites with steam and

bubbling liquids are found at CO_2-poor and/or water-poor ratios in comparison to H_2S concentrations. The field of data for TGS Multigas lies within the field for hydrothermal gas results from around the world (Fig. 2) (Aiuppa, 2015; Aiuppa et al., 2016; Lages et al., 2020).

The sampled n = 2 fumarole gas samples (one each from JM and PS) are dominated by CO_2, which comprises >81.5% of the total gas in each sample using acidimetric titration (Table 2). For the hot spring gas, samples PB (1,2,3) (PS site) reach the maximum of 0.72% N_2 (3.6% in Tardani et al., 2016), while the well samples have only 0.52% (Table 2). In contrast, the wells have a maximum of 98.0% CO_2, and 21.5–23.6 ppmv carbon monoxide (CO) but relatively low methane (CH_4=<625 ppm). Methane concentration reaches 3172 ppm at PS compared to ~300 at the JM fumaroles, with major differences observed at the northern fumaroles (5420-24200 ppm) in comparison to the lowest values in the southern sector (130–180 ppm) which had been previously detected by Melosh et al. (2012). The H_2S was measured by iodometric volumetric titration, giving values of 14.1% for PS, 1.1 % for JM and 0.86–0.91% for the wells. Melosh et al. (2012) found in addition that the northern discharge sites were richer in H_2S (5.27–11.2%) compared to the southern sites (0.55–2.7%).

The majority of the PS fumarole and hot spring gas samples (Table 2) have O_2 contents lower than 0.4% (<68 ppm in wells). All fumaroles sampled have much higher N_2/O_2 values than that of the air ratio of 3.73, suggesting only weak atmospheric contamination (PB < 120; JM <90). Published helium isotopic data by Tardani et al. (2016) showed that the gases were not strongly affected by atmospheric helium. All of our samples in this study showed traces of He (>7ppm), suggesting minimal contamination during analysis, and, for reference (Tardani et al., 2016), the $^4He/^{20}Ne$ ratios (16.1) from the same sites do not coincide with the air ratio (0.33).

4.2 Petrochemistry of Tolhuaca post-glacial magmas

The bulk rock chemistry compositions are presented in Table 3, with spidergrams illustrating the rock compositions in Supplementary Material figure S2. Outcrop locations for rock samples at Tolhuaca are shown in figure 1c. The Cono Canción (CC) has three samples (CC1, N12CC, CC12022) which all have a porphyric texture, containing around 40 to 45 vol. % phenocrystals in a vitreous, microcrystal-rich groundmass. Phenocrysts are plagioclase (24–27 vol.%; normally to inversely zoned; An_{46-58}), olivine (10–11 vol.%; (normally zoned; Fo_{66-78}), clinopyroxene (4–3 vol.%; inversely zoned; $Wo_{41–43}En_{44–46}Fs_{9–14}$), orthopyroxene (1–2 vol. %) and opaque minerals (0.5–1 vol. %). The groundmass contains > 30 vol. % of phenocrysts, including olivine**.** There are abundant crystalline clusters (cumuloporphyric texture) of plagioclase, olivine, pyroxenes, and opaque

minerals. The mineral-MI corrected PEC pairs demonstrate the least primitive Mg endmember in comparison to other MEC (n = 6; Fo<73%; Fig. 3a). The plagioclase occurs as phenocrysts of andesine and anorthoclase, while the matrix crystals are anorthite.

The bulk rock samples at CC span basaltic to andesitic compositions (SiO_2=57.8–60.1 wt%, K_2O=1.2–2.00 wt%, MgO=3.2–4.1 wt%) (Fig. 3b). Trace-element rock contents exhibit a slight enrichment in light rare earth elements (LREE) in comparison to the heavy rare earth elements (HREE), close to a typical MORB signature (Table 3; Figure S2). This enrichment appears to be more marked in TF, in agreement with regional literature data from Lonquimay (Vergara and Lara, 2010). The range of La/Yb is used to compare this enrichment in an L-HREE spidergram and to evaluate possible effects from garnet fractioning, for example; it can be seen that CC exhibits few variations (5.38–7.27) (Figure S2). In terms of the trace elements, the rocks are slightly enriched in large-ion lithophile elements (e.g., Cs, Rb, Sr, and Ba) relative to N-MORB. Most samples have low contents of the high-field-strength elements (HFSE) Ta, Nb, Zr, and Hf. Sedimentary incorporation into the mantle is identified using “geomarkers” (Robidoux et al., 2021). Here we have used Ba/La, Th/La and U/Th ratios, which indicate sediment and fluid components from the subducting slab (Plank, 1998), giving values of 2.3–34.6, 0.09–0.53, 0.12–0.43, respectively (Table 3). All of the MEC demonstrate extreme minimum and maximum values for Ba/La, apart from CC for which U/La and U/Th clearly have consistent high ratios of 0.33–0.53 and 0.28–0.31, respectively. An additional crustal geomarker, the Sr/Y ratio (Chiaridia, 2017; Robidoux et al., 2020), shows a range of 8.9–41.4, with the maximum at CC (41.4).

The Tolhuaca Fissure (TF) group represents five samples from different sites along the km-long linear structure (FI1A, TO1B, TO1A, TOL-01, including NV18 provided by N. Vinet). They are compositionally heterogeneous, ranging from basalts to basaltic andesites (SiO_2=~53.5–59.3 wt%, K_2O=0.9–1.4 wt%, MgO=3.8–6.3 wt%). The trace and REE record similar trends to other MEC, but the La/Yb and Sr/Y ratios are variable (3.61–12.5 and 1.7–17.9, respectively). Samples have a porphyritic texture in a densely microlithic-rich groundmass, with 30 to 35 vol. % of phenocrysts; plagioclase (normally zoned; An_{48-73}), olivine (normally zoned; Fo_{65-82}) and ortho- and clinopyroxene phenocrysts (normally zoned; $Wo_{32–39}En_{30–42}Fs_{24–31}$). The groundmass contains an abundance of plagioclase (> 50 vol. %), as well as orthopyroxene and opaque minerals. The samples have small crystalline clusters (cumuloporphyric texture) of plagioclase, orthopyroxene, olivine, and opaque minerals. A number of crystals were selected from the samples for EMPA, which showed the olivines to be heterogeneous in composition ($Fo_{81–85,}$ Fo_{83}±2%; Fig. 3a), the plagioclase to be anorthitic, and the pyroxene to be augite with a high Mg content that is slightly under mineral-glass equilibrium values (Mg# of 78–83; *average value of?* Mg#80.5±2.5%).

The Cono Caracol group contains two samples (CAO4-A, CA02A) and the Cono Coli group three (COO1B, CO03, COO2), sampled from the SW flank of Tolhuaca. The samples from Cono Caracol have a porphyritic texture with >30% vol. of phenocrysts in a highly vesicular groundmass, with large, uniformly-oriented vesicles (> up to 1 mm). Interstices are filled with microliths and glass, observed under the SEM to have the same orientation as the vesicles (pilotaxis and hyalopilitic texture). The phenocrysts are mainly plagioclase and pyroxenes, both with coronitic textures. Selected crystals used for EMPA shown that the olivines in Cono Caracol had similar compositions to those in the TF group but were less heterogeneous in forsterite ranges ($Fo_{79–82}$, $Fo_{80.5}$±1.5%Fo; Fig. 3a). The trace and REE are similar to the other Tolhuaca MEC, although La/Yb is slightly lower, for example Cono Caracol have low ratios (~3.65–5.79), and Cono Coli moderate values (4.89–9.61). The samples from Cono Coli also have a porphyritic texture with >30% vol. of phenocrysts in a highly vesicular groundmass, but here the vesicles are not aligned. Instead, there are rim replacements by epidote on opx and cpx minerals, making it impossible to carry out MI studies and mineral chemistry on this set of samples.

4.3 Thermobarometric and compositional magma reservoir constraints

The post-entrapment corrections (PEC) on glass inclusions made in Petrolog 3 (Danyushevsky, L. V., & Plechov, 2011) are presented in Table 4, with normalized and augite-liquid pairs and PEC treated glasses in Table 5 using respective P-T condition estimations. The data treatment takes into consideration the diffusion exchange of FeO and MgO along the walls of the inclusion and the olivine host, then the Fe loss from the inclusion into the olivine host for which vol. % olivine or augite are added (uncorrected MI provided in Supplementary Material Table S3; original glass rim composition in Table S4). The plagioclase-liquid pair compositions are reported in Table S5.

The MI from CC are classified as dacites and trachydacites following PEC treatment (SiO_2 = 69.2–70.9 wt.% and K_2O=0.64–0.82 wt.%) and are classified as high-potassium calc-alkaline (HKCA) rocks (Fig. 3b). The MI from TF are classified as basalts (TOLB9) and basaltic andesites, with a large range of compositions (SiO_2 = 45.8–55.5 wt.% and K_2O=2.53–4.60 wt.%). The Cono Caracol has one well-preserved MI of dacitic composition (SiO_2 = 63.4 wt.% and K_2O=2.52 wt.%). Only four inclusions were classified as augite mineral phases and these had FeOT values higher than the FeOT vs MgO trend of their host rocks. These inclusions are classified as basaltic andesite melts (SiO_2 = 53.8–54.9 wt.% and K_2O=0.69–0.80 wt.%).

Under hydrous conditions, using the first-round iteration of H_2O wt.% contents for the MI, the anorthosite-liquid pairs match T<1050 °C for $KD_{Ca\text{-}Na}$ = 0.25±0.05, resulting in a pressure range of 14.6–19.9 kbars. After the second iteration, using Lange et al. (2009)

water content estimations (0.43–1.63 wt.%, lower than our measured SIMS contents of 1.77 wt.% H_2O), the equilibrium temperature range for T<1050 °C is 1003–1047 °C, giving a pressure estimation of 14.9–19.2 kbars (Fig. 4b). For anhydrous conditions, the geothermobarometer gives higher equilibrium temperatures for andesine-liquid pairs (1050–1060 °C), producing equilibrium pressure values of between 1.52–3.88 kbars; this dataset fits most of the MI volatile saturation pressures for CC, therefore the olivines and andesine phenocrysts crystallized synchronously. The anorthoclase series, in comparison, only show n = 6 samples in equilibrium under dry conditions, giving temperature and pressure ranges of 1035–1049 °C and 16.6–20.7 kbars respectively.

The olivine-glass pairs were used as best-proxies for the primitive residual melt composition, but the olivine composition was heterogeneous. The glass rims around augites from CC are classified as dacites, rhyodacites and rhyolites (Table S3; Fig. 3b), with higher K_2O (2.43–3.59 wt.%) and SiO_2 (66.5–69.7 wt.%). The n = 6 glass rims around olivines plot around the same regions in the Bas et al. (1986) diagram, but with much lower minimum values (SiO_2 = 54.7–68.2 wt.%; K_2O = 0.32–4.32 wt.%). The n = 19 glass rims for augites from TF are classified as basaltic andesites and andesites (Table S3; Fig. 3b), with moderate K_2O (0.50–1.45 wt.%) and SiO_2 (54.3–55.7 wt.%). The n = 8 glass rims around olivines are similar in composition but have lower minimum contents of incompatible elements (SiO_2 = 44.7–57.5 wt.%; K_2O = 0.18–1.36 wt.%). Two olivine-glass pairs from Cono Caracol have basaltic compositions (SiO_2 = 42.9, 44.6 wt.%; K_2O=0.67, 0.70 wt.%).

Glass inclusions used for the augite-liquid pairs at TF were treated for PEC and the H_2O content from SIMS analysis (1.40–1.48 wt.%; TOL1A29) was used to estimate MI entrapment pressures under hydrous conditions and adjusted $KD_{Fe\text{-}Mg}$ to 0.26. The resulting equilibrium pressures and temperatures give respective ranges of 4.9–5.3 kbars and 1182–1186 °C for hydrous conditions, and 3.9–4.3 kbar at 1182–1186 °C for dry conditions. The non-PEC treated data (glass rims) were used to estimate P-T parameters at late crystallizing stages (Fig. 4b), assuming matrix-glass water content measured from SIMS of 0.14 wt.% (sample TOL1A104). To agree within $KD_{Fe\text{-}Mg}$ = 0.27±0.03, core or rim spots matching MI were probed for hydrous conditions resulting in pressures and temperature of 0.6–8.8 kbars and 1149–1205 °C respectively; dry conditions range from 0.5–8.7 kbars and 1149–1205 °C respectively. The augite glass rims were probed (including PEC-treated sample TO1A29), with conditions resulting in pressure and temperature ranges of 0.7–8.8 kbars and 1149–1206 °C respectively; dry conditions range from 0.6–8.7 kbars and 1149–1206 °C respectively.

4.4 Magma volatile-fluid mixture

The volatile contents for MI determined using SIMS and geothermobarometric conditions are shown in Table 6, and noble gas analyses for FI in Table 7. The volatile contents for MI are given only for inclusions of glassy texture, without observable post-entrapment effects (they are bubble-free and there is an absence of MI-crystal host reaction rims), except for two glass samples (microlith-free) measured in contact with mineral glass borders used to represent degassed MI endmembers (glass borders or hourglass MI typology; CC1l1c7v5, TOL1A104v). The Tolhuaca inclusions with the highest volatiles are the TF group (1.94 wt%), compared to the rest of MEC samples (<bdl; 0.14–1.77 wt%) (Table 6; Fig. 4a). The MI sample from Cono Caracol is close to levels that are below detection limits (bdl) for most volatile contents, therefore it is not considered suitable for further discussion, apart from for sulfur species measured by EMPA. In terms of CO_2 content (Table 6; Fig. 4a), the TF inclusions again have the highest value (2496 µg/g) relative to the other MEC samples (<bdl; 79–188 µg/g), but despite this high value, it represents an outlier in comparison to the typical low volatile contents of this series.

The S, Cl and F contents at Tolhuaca MEC are heterogeneous with the following ranges, respectively: (6–497 µg/g), (376–1095; anomalous spot at 4008 µg/g) and (70–508 µg/g) (Table 6). The S content calculated using EMPA (Table 4, 5) with numerous repeated spots on mineral-MI pairs (n = 37), all show low contents at the CC, TF and Cono Caracol MEC, respectively; (75–509 µg/g), (21–537 µg/g) and (148, 232 µg/g; with n = 2 spots at Cono Caracol). The sulfur contents all have similar maximum values, so this value is not expected to exceed ~500 µg/g in preserved melts from Tolhuaca MEC olivine-hosted inclusions.

Fluid inclusions from five samples (in which sufficient olivine crystals were available for separation and isotope analyses) from Tolhuaca MEC were analyzed for noble gases: He, Ne and Ar. The ^{4}He concentrations measured in FI from olivines of scoriae samples varied from 1.94×10^{-15} to 3.52×10^{-14} mol/g (Fig. 5abc). Ne (^{21}Ne, ^{22}Ne) and Ar (^{36}Ar, ^{40}Ar) in the olivines range from 9.47×10^{-17} to 3.49×10^{-16} mol/g and from 3.50×10^{-13} to 1.88×10^{-12} mol/g, respectively. The $^{40}Ar/^{36}Ar$ ratio was 299–320 in all samples (Table 7), which is slightly higher than the atmospheric signature ($^{40}Ar/^{36}Ar$ = 295.5). Similarly, $^{4}He/^{20}Ne$ was higher than the atmospheric value (1.4–18.7 compared to 0.318, respectively) (Fig. 5ab**)**. Both $^{40}Ar/^{36}Ar$ and $^{4}He/^{20}Ne$ indicate that gases released from FI contained a component derived from the atmosphere.

The $^{3}He/^{4}He$ ratios (expressed as Rc/Ra values) (n = 5) vary between 5.44 and 6.9 Ra without corrections, and 6.28-8.16 with corrections (6.96 ± 0.81 Ra) for olivines (Fig. 5a,c). Previous volcanic gas studies (Lages et al., 2021a,b and references therein) in the CVZ considered $^{3}He/^{4}He$ lower than 6.4 Ra to be representative of the magmatic source at Villarrica, but volcanoes that are closer to Tolhuaca such as Lonquimay and Llaima only reach 4.4 and 6.93 Ra (Hilton et al., 1993), with a maximum peak of 8.42 Ra for Copahue (Roulleau et al., 2018; Tardani et al., 2021). The large range for this ratio

indicates that few Tolhuaca gas samples are affected by crustal ^{4}He given the heterogeneous dataset from literature in CVZ and SVZ (4.01–8.42). The range of $^{3}He/^{4}He$ at Tolhuaca peaks at 8.20 Ra, which is within MORB-like values (R/Ra = 8 ± 1; Graham, 2002).

5. Discussion

5.1 Controls on shallow gas component from vapor zone to the geothermal field

As seen from the results for the fumarole sites in the PS-JM sector, the CO_2-H_2O-H_2S gas composition, particularly the CO_2/S_t ratio, is consistent with other hydrothermal gas systems in the literature (Fig. 2). However, the distribution of CO_2/S_t ratios at Tolhuaca requires further explanation. The wells sampled at Tolhuaca range from 107–113 (southern sector peak of 170.9; Melosh et al., 2012), comparable to JM ratios (86.5) by direct sampling with the Giggenbach method (Tardani et al., 2016). Lower values are reported at PS (5.8), comparable to the range recorded by Melosh et al., (2012) for the northern sector (7.2–10.5). Based on this, we investigate whether the temperature and type of discharge site might explain the variation in gas composition (Fig. 6ab).

The inverse temperature correlation commonly observed for volcanic gas CO_2/S_t ratios (Aiuppa et al., 2012, 2014; Fig. 6a) suggests a possible control might exist between the northern and southern sectors for the vapor gas component at depth. However, spatial temperature changes at surface TGS show no spatial pattern and are uniformly fairly low (96.5°C; Collignon et al., 2021), making it difficult to test for temperature dependence, given the low temperatures of our samples (~<96°C). Thus it is not possible to model high-temperature sulfurous gas mixtures as has been done for magmatic vents elsewhere (Aiuppa et al., 2014, 2017; Ding et al., 2023), and which could be the case in certain open-vent volcanic systems or other hydrothermal fields from the Andean Cordillera (Lascar, Lastarria, Alitar, Copahue-Caviahue; Tassi et al., 2011; Agusto et al., 2013; Tamburello et al., 2014; Lopez et al., 2017). For instance, some systematic temperature changes are seen at Alitar, northern CVZ (fumarole system with no boiling water) which has CO_2/H_2S values of 37–81 at 85°C, but reaches 755–819 for fumaroles that record lower temperatures (54–57 °C; Tassi et al., 2011). At Copahue, prior to most of the hydrothermal fields being flooded by a lake (current $CO_2/S_t < 6.4$; Tamburello et al., 2014), the surficial manifestations recorded the highest temperatures (>96°C) and highest 109–124 range for CO_2/H_2S fumaroles (250–300°C using geothermometers from gas at a depth of 800–1,000m in the hydrothermal reservoir; Barcelona et al., 2020), contrasting with ratios of 5–115 (<96°C) at bubbling pools where the molar fraction of water is <33.7% (Agusto et al., 2013). For Tolhuaca (Fig. 6a), based on our modelled gas thermometer (Powell et al., 2010; Fig. 6ab), the southern sector is in equilibrium with higher

temperatures (equilibrium for wells at ~350°C) than the northern sector (150–200°C), therefore the PS sector could be farther from the heat source, assuming it is beneath Tolhuaca, but far from most MEC vents and exploration wells (Fig. 1c). In comparison, JM site is closer to identified MT magmatic storage location few hundred meters closer to Tolhuaca summit (Pavez et al., 2022).

In many of these CSZ and SVZ geothermal systems, the heterogeneity of gas mixtures could be linked to the type of discharge site (for example, dry fumarole or boiling water, e.g., Agusto et al., 2013), and explain the local variation of gas flux composition. Dry and diffuse fumaroles at Tolhuaca do not exceed H_2O/CO_2 ratios of 6.0, despite most of these vents recording the highest CO_2/S_t ratios (>94.0), while bubbling pools show heterogeneous results for H_2O/CO_2 and H_2O/H_2S ratios (Table 1, S1). This observation (Table S1) appears plausible, as depending on the individual type of discharge site, we found some evidence of localized gas mixture variations from our Multigas and direct gas sampling, as at Copahue (Agusto et al., 2013).

The geographic variation in CO_2 flux could explain TGS differences in terms of the major gas species. We compare the gas ratio distribution at JM (on the upper flanks) with PS (on the lower flanks) with the CO_2 surface mapping of Collignon et al. (2021). Our dataset confirms an average CO_2/S_t ratio at JM (141 err. STD±58) that is much higher than at PS (53 err. STD ±24). This confirms that CO_2 is the dominant gas in the JM sector. On the other hand, the CO_2 flux from Collignon et al. (2021) is lower in the JM sector (0.77±0.22 t/d; T <96.5 °C) compared to the PS sector (3.13± 0.47 t/d; T <90.0–95.5 °C), confirming the relative variation in molar content of other gas species in CO_2-rich flux sources.

To explain the origin of the Multigas dataset variation, we use the gas chemistry of fumaroles to evaluate the influence of the magmatic source using ternary gas solubility calculations in a CH_4-CO_2-H_2S system (Tcch; Powell et al., 2010). The CO_2-rich fluid at JM is confirmed as being connected to magmatic-gas values (<200–350 °C; Fig. 6b; Powell et el., 2000, 2010), based on the fact that volcanic gases generally have high CO_2/CH_4 ratios (Giggenbach, 1996). The Tol-1,2,3 well ratios reach values of 1,568–1,915 (Melosh et al., 2012), the ratios for the JM sector range from ~5,222–7,169, with a peak value of 317,400 (Rc/Ra ~6.5 confirm it to be typically magmatic; Dobson et al., 2013; Tardani et al., 2016). In contrast, the samples from the PS sector diverge from magmatic-gas values (Fig. 6b), (CO_2/CH_4 = 257–283; ~32.8–148 in Melosh et al., 2012). The reason for lower CO_2/H_2S ratios in this sector could be that the gas mixture is weakly controlled by absorption of sulfur-bearing gases (H_2S) into the shallow aquifer (e.g. Taussi et al., 2023). In addition, the CO_2/H_2S ratio could increase when the H_2S species is stripped from the system by subterranean water (Giggenbach, 1996), which would also affect other highly dissoluble gas species (HCl, HF, SO_2, SO_3, H_2SO_4, etc.).

The effects of the hydrothermal system on the surface gas mixture composition are now looked at in terms of the geological context, along with additional information from gas well surveys (Fig. 1c, 4b; see figure 8 in section 5.3). We suggest that steam-heated water above the argillic conductive zone (at a depth of 20–400 m in drill holes; Melosh et al., 2010, 2012; Sánchez-Alfaro et al., 2016) could have a major stripping effect of H_2S in the southern sector before the gas mixture reaches the surface. The location of the JM sector in a collapsed amphitheater structure (Fig. 1c), with its NE fracture system typical of regional LOFS structures (Tardani et al., 2016; Pérez-Flores et al., 2017a), represents a plausible permeable outlet zone for the Tolhuaca geothermal system (e.g. White et al., 1971 model), in which water is naturally filtered through numerous porous, fractured rock layers above the conductive zone (detected by geophysics, e.g. Melosh et al., 2010, 2012; Pavez et al., 2022), favoring mixing of meteoric water with deeper boiling magmatic gas (e.g. identified by reported well gas studies; Melosh et al., 2012; Pokrovski et al., 2013; Sánchez-Alfaro et al., 2016).

A major difference also exists in terms of air contamination, with variation in contents of O_2 and N_2/O_2 ratios indicating that the means of transport may differ between the JM and PS sites. For example, air contamination at PS is more marked in our new gas dataset (CO_2/Ar = 3,400-7,800) in comparison to JM sector (CO_2/Ar > 17,700-33,200; Tables 1, 2), showing that the deep gas mixture at PS carries traces of greater atmospheric mixing as opposed to hydrothermal interaction since the latter would affect dissoluble gas species (e.g. H_2S). Sampling by Melosh et al. (2012) near to PS and the northern sector fumaroles (Fig. 1c) also revealed that the "CO_2-poor gases" (low CO_2/H_2S) at surface vents are oxidized. As H_2S is better preserved in the PS area (Fig. 2, Table 1,2), we infer that meteoric water infiltrated into the rocks and mixed with deeper H_2S-rich fluids flowing upwards from the vapor zone, limiting dissolution of H_2S in the lower NW sector. Since the altered resistivity cap appears closer to surface in the northern sector (Melosh et al., 2012; Sánchez-Alfaro et al., 2016; Pavez et al., 2022), one possibility for restricting early H_2S stripping could be related to the prevention of meteoric water infiltration and early mixing with deeper H_2S-rich fluids flowing upwards from the vapor zone (see model in figure 8).

Low CO_2/H_2S ratios (<18.0) are reported at the fumarole sites just beyond the flanks of Tolhuaca, measured with the Giggenbach method (Pemehue Pelehue, Banos del Toro at Sierra Nevada; Tardani et al., 2016). This may indicate that in addition to a lower diffusive CO_2 flux, low-temperature (<93°C) water interaction favors carbon dissolution over H_2S dissolution in the hydrothermal system (instead of pure H_2S scrubbing; Symond et al., 2001). Further water chemistry studies are required to confirm this hypothesis, but there is evidence to believe that the CO_2-H_2S interplay is enhanced by mineral-fluid reactions involving deep geothermal gas sources (Arnórsson, 1986). We thus believe that the high CO_2/H_2S ratios in the JM sector could be related to plagioclase-

rich rock dissolution in the presence of CO_2-rich fluids with less H_2S involvement, as has been recorded elsewhere in the SVZ (Sánchez-Alfaro et al., 2013, 2016; Tardani et al., 2016; Wrage et al., 2017; Daniele et al., 2020), leading to an increase in HCO_3^- in geothermal waters.

5.2 Magmatic fluid ascent and evolution during ponding

To evaluate the conditions of magma storage, ascent, and degassing during the Tolhuaca syn-to post glacial eruptive history, the volatile contents of glass inclusions and their major-element concentrations (in wt.% in figure 4) were compared with values from SVZ samples in the literature and model simulations of volcanic degassing in figure 7 (in mol.%). In this dataset, volatile contents from the strongly pressure-dependent H_2O–CO_2 system in MI reached maximum values of 3.11 wt. H_2O and 305 ppm CO_2 (Bouvet de Maisonneuve et al., 2012; Pioli et al., 2015), making them suitable for geobarometric calculations (Moore, 2008), for example in Chile, at Villarrica volcano (Chaimilla deposit), Llaima and Callaqui (Rea, 2009ab). In Tolhuaca, despite all samples being treated for PEC (n = 22), including volatile-bearing MI, the low water content (<1.9 wt.%) is indicative of volatiles being lost by diffusion and degassing prior to entrapment (Fig. 4a; 7ab).

The PEC effects identified for the H_2O–CO_2 system also appear to lower the values for the S–Cl system measured in our study (~48–1,258 ppm S and ~70–508 ppm Cl) in comparison to ranges for SVZ and CVZ volcanoes (34–3,201 S and 257–1,582 Cl ppm), indicating that our MI have undergone degassing prior to entrapment. Based on the most prolific dataset to date (16 volcanoes), MI from the SVZ exhibit Cl and S abundances in the same range as most of those from the Central American and Marianas arcs (Wehrman et al., 2012, 2014). Weller and Stern, (2018) recently extended the area of study to the southernmost part of the SVZ by integrating S-Cl datasets from Pleistocene-to-Holocene volcanoes (594–1,430 ppm S; 125–777 ppm Cl) at Hudson, Macá, and Melimoyu, reaching maximums at Mentolat volcano (1,227–2,656 ppm S and 704–1,078 ppm Cl).

We used the SolEx software (Witham et al., 2012) to approximate degassing paths for Tolhuaca magmas (TF, CC) and calculate the equilibrium compositions of coexisting melt and vapor phases over a range of pressure and temperature conditions relevant to the system (Figs. 4ab). The saturation model derived from D-Compress uses the H–O–C–S–Cl–Fe system from the melt, incorporating our estimated range of fO_2 (-7.9 to -8.1 at TF and -9.9 at -10.1 at CC) derived from our FeO/Fe_2O_3 titration dataset (Table 2) and P-T-fO_2 interdependence from the Kress and Carmichael (1991) model.

Three sets of model runs were carried out with measured volatile contents starting with “Primitive Melt: Tolhuaca Model” (Figs. 4a). We note that the PEC-treated MI from the TF series had 0.4 wt.% lower parental melt H_2O contents (Fig. 4a), thus the

near-vertical closed and open system degassing paths involves samples affected by water diffusion, since most SVZ and CVZ magmas have higher initial maximum H_2O contents (e.g. Villarrica; 3.11 wt.%; Pioli et al., 2015). The second model “Primitive Mantle Model” represents a hypothetical mantle-like volatile mixture, which can be used under plagioclase-liquid equilibrium hydrous conditions with 4.0 wt.% H_2O (from Putirka et al., 2005). The third model “Cono Canción Model» considers maximum volatile contents measured in this MI series. Although the degassing paths exaggerate trends, they provide a range of mantle-derived water contents that are typical of volcanic arcs (~4.6 wt. % H_2O; Plank et al., 2013).

To highlight the contrast in the CC and TF melt-volatile mixtures during transport, the individual measured MI volatile abundancies are modelled in figures 7 a-b with uniform scientific units (X mol.%) to predict CO_2/S_t composition during magma decompression, with the aim of estimating the composition of the gas mixture of an ascending or ponded magma below Tolhuaca. At JM, close to the CC sites, a volatile saturation depth range of 0.9 to 3.2 km would produce a gas phase that separated from the magma, at a minimum depth of 1.1 km for the volatile mixture to fully diverge from parental melt compositions, based on CO_2/S_t ratio variations during decompression (Fig. 7ab). Interestingly, boiling events at a depth of 0.95 km have been identified from well studies (Sánchez-Alfaro et al., 2016), thus this depth marks the minimum estimated pressure for CC to separate off the magmatic volatiles at <60 meters from the magma saturation level (Fig. 4a; Table 3, 4). According to the model of high-enthalpy geothermal systems, a thin layer thought to be less than a few hundred meters (Arnórsson et al., 2007) exists between the magma and the base of the convection hydrothermal fluid, through which heat from the magma is transmitted. We suggest that the melt-saturation level could be a key parameter for geothermal exploration. If emitted gases represent an equilibrium fluid at depths down the vertical plumbing system (Burgisser et al., 2015), it is possible to deduce the pressure of equilibration of a gas emitted from a volcano from the CO_2/S_t ratio (Burton et al., 2007). Here we test such a model for the Tolhuaca magmas. Using these conditions, we have plotted pressure profiles in figures 7ab which show a striking change in CO_2/S_t molar ratios from gases which requires further investigation.

The change in degassing volatile-mixture composition occurs at 500–300 bars, as observed from the CO_2/S_t using xH_2O molar ratios (Fig. 7ab). Considering sulfur does not affect the behaviour of the volumetrically dominant CO_2 in the melt (Wallace and Carmichael, 1992), the CO_2/S_t evolution in our three degassing models (Fig. 4ab) is largely controlled by the individual melt behavior of CO_2 and depends mainly on the solubility model (Moretti and Papale, 2004; Witham et al., 2012). This pattern is also found at low pressure (<1,000 bar), because sulfur decreases in abundance due to the pressure dependence of its partition coefficient, Ks (Lesne et al. (2011a). The trend of sulfur melt

content during decompression diverges below 500-1,000 bars (Fig. 7a), because of the large amount of exsolved CO_2 at low pressures and the Ks behavior reducing dissolved S as modelled using SolEx software (Whitam et al., 2012). The last explanation for the degassing models, from 1,500 to 300 bars, is that the open system diverges from a closed-system, principally because degassing at low pressure releases mainly H_2O, which dominates the gas composition (Fig. 7b).

Under these conditions, magmatic activity acts as a hypothetical gas mixture source in which SO_2 is the dominant sulfur species that separates off into the vapor (Shi and Saxena, 1992). Therefore, we infer that at Tolhuaca the gas sulfur species is reduced because it has been undergoing reaction in the subterranean environment since the post-glacial era (6 ky; Polanco 1998, 2000; Moreno Roa and Gardeweg 1989). Considering the diversity of physical and chemical barriers (surficial, oxidation, water stripping reactions to convert magmatic SO_2; Giggenbach, 1996), we also note that the geothermal vapor produced and described in previous section will be subject to modification. In addition, when evaluating the degassing at Tolhuaca, the sulfur species from the melt are considered as three species in the D-Compress solubility model ($S_t = SO_2 + H_2S + S_2$). By strictly converting our MI composition from volatile-rich MI with the D-Compress model (sample CC1m65; 911 bars), the CO_2/S_t ratio is 0.002 (Fig. 7a), which corresponds to $4 \cdot 10^{-5}$ H_2S/SO_2. If the CO_2/S_t ratio only considers H_2S (supposing all magmatic SO_2 is converted to H_2S following oxide-reduction equilibrium with iron from the melt; Burgisser et al., 2015), near-atmospheric pressure conditions for the ratio of the magmatic gas mixture gives $CO_2/H_2S = 50.5$, which is within the standard deviation range of Tolhuaca surface hydrothermal ratios (CC; 83–199; PS 29–77). If the TF magmatic gas CO_2/S_t ratio is 0.8 (modelled with our MI sample Tol1a_29; P = 688 bars), the magmatic gas mixture becomes $CO_2/H_2S = 31.1$, which also lies within the total range for TGS (Fig. 2, 7ab), as for other regional SCVZ water-dominant systems measured with Multigas/Giggenbach methods (Copahue-Caviahue, Irruputuncu; Tassi et al., 2011; Agusto et al. 2013; Tamburello et al., 2014) (>95 xH_2O%).

5.3 Magmatic and fluid source characteristics

The magmatic vents close to the TGS provide evidence of a close connection to primitive mantle compositions for magmatic fluids and present-day geothermal systems, as shown by a review of whole rock analyses in combination with isotopic noble gas analyses (Fig. 4,5,6,7).

The roots of the Tolhuaca MEC magma feeding system indicate crystallization of anorthoclase at 53–69 km, followed by andesine at 5–14 km, thus it is possible to model transport through the entire depth of the continental crust from the mantle to surface

(continental crust thickness ~<60 km; Tassara and Echaurren, 2012). In comparison, silicate melts were entrapped in olivine at a minimum of 0.9 to 3.2 km (Fig. 4), with ~3 km being a sufficient depth (Scott et al., 2015a; Fig. 8) for the fluid pressure above the hypothetical CC intrusion to exceed the critical pressure necessary to produce hot water to circulate as convection cells (Fig. 8). If the magmatic fluids are not associated with a dacitic CC magma source, but rather the basaltic TF endmember, then augite will crystallize and preserves volatiles at 2.1–21.9 km. If the TF were to be the source of the magmatic gas, it would reach saturation levels between 2.01 to 2.48 km based on solubility models with olivine hosts, which also corresponds to these critical pressures (Fig. 7ab; Fig. 8).

The presence of olivine in CC (Fo_{73}; Fig. 3), despite exhibiting normal zonation and low-volatile-content entrapped FI, supports modified atmospheric vs. mantle mixing ($^4He/^{20}Ne$) due to the minimal effect of helium loss and ^4He radiogenic addition to the preserved fluids (Fig. 5a, c). Bulk rock evidence from trace and REE geomarkers (such as the high Sr/Y ratios; Chiarida, 2015; Robidoux et al., 2020) demonstrate crustal interaction which lowers the Rc/Ra (<7.0, which is not representative of the mantle source), for which the ^4He addition appears to be a plausible explanation. The consistently high U/La and U/Th ratios, an indication of slab fluid sediment incorporation, demonstrates that the mantle-fluid signature (Fig. 8, S2) has had a greater impact on the CC samples than at other MECs (Fig. S2). Evidence of crustal ^4He addition demonstrates that the mantle-fluid signature at Tolhuaca has been lost at CC, despite high 6.49±0.05 Ra from fumaroles near this volcanic vent (Tardani et al., 2016). The magmatic fluids produced at CC, as all along the TF structure, likely feed geothermal sites on the flanks of Tolhuaca, and thus no recharge by new mafic magma is necessary to maintain this signature at hydrothermal sites under present-day conditions (Fig. 8). Given the conditions at depth through which the magmatic fluids were transported to the TGS (Fig. 5, 7), we infer that the magma interaction with the crustal plumbing system would strongly affect CC and that TF could derive from the same mantle source. The noble gases in FI from compositionally-heterogenous olivine crystals ($Fo_{65–82}$) from TF exhibit a local peak in $^3He/^4He$ ratio of 8.20 Ra in the region with the most MORB-like magmatic source (8 ± 1 Ra; Graham, 2002), as observed at Copahue (Roulleau et al, 2016). Olivines with intermediate forsterite contents ($Fo_{79–82}$; Fig. 3) are also observed at Cono Caracol, which has weak evidence of atmospheric vs. mantle mixing ($^4He/^{20}Ne$) and some degree of helium loss in comparison to TF (Fig. 5, 8a).

TF appears to be the best “parental" melt candidate as it has the highest volatile content, as well as the highest CO_2 content in FI analyses (Table 7). The $CO_2/^3He$ ratio is used to identify the effects of both degassing and crustal contamination on the preservation of volatiles within host minerals (Fig. 9a). A crust-mantle mixing model is used to reproduce such effects (Lages et al., 2021b; Taussi et al., 2023), which also apply

to regional NVZ and CVZ volcanoes. There is broad evidence of marine sediment input via subducted fluids to explain the excess radiogenic He and carbon, but TF magmas have the most primitive mantle signature. Here there is no clear evidence of crustal contamination within the plumbing system since the $^{3}He/^{4}He$ ratios measured in FI are higher than any others found at this volcano, markedly higher than those previously reported for fumaroles (6.49 Ra) (Tardani et al., 2016) (Fig. 9a). This indicates that fumarole gases near the summit of Tolhuaca (JM sites; Tardani et al., 2016) become weakly contaminated within a shallow hydrothermal system by crustal rocks or fluids bearing radiogenic ^{4}He before being released at the surface (Snyder et al., 2003; Shaw et al., 2003). The actual TGS, particularly at JM site is closer to representing the magmatic-fluid source (Rc/Ra, CO_2/H_2S; CO_2/CH_4). This evidence all points to a magmatic body below or even near to CC (Pavez et al., 2022) that is still connected to the local geothermal field, which channels primitive mantle fluids that traversed the crust (and hydrothermal bodies) subject to only limited crustal contamination along the way (Fig. 9a).

Independent of the processes that affect $^{3}He/^{4}He$ at fumaroles, our study of FI finds that the magmatic source has remained constant over time since the Holocene, and over different depths of the plumbing system (Fig. 8). Regionally, it also means that the mantle has conserved a primitive MORB signature, even at a distance from the slab (e.g. Copahue; Roulleau e tal., 2016, 2018), therefore modification to bulk rock chemistry is not necessarily due to mantle heterogeneities, but to local factors that modify the primitive signature of typical slab fluid (U/Th, Ba/La; Ba/Nb, etc.; Fig. 9b and Fig. S2).

The $^{3}He/^{4}He$ signature of Tolhuaca magmas is here looked at within the framework of other CVZ volcanoes, using U/Th (Fig. 9b) as an indicator of slab input (Giggenbach, 1993), and, more specifically, sediment input from the Nazca Plate to South American magmas (e.g., Lange et al., 2021ab and references therein). It is well documented that U/Th, as well as other key ratios, shows large variations within the Andean Cordillera (reflecting changes in the dip of the subducting slab), whereas the steepest dip in Central Chile induces intensive metasomatism and lower degrees of melting in the mantle. These results in the melt generated from the mantle being heavily imprinted with the signature of the subducted slab (i.e., high U/Th and Ba/La). On the other hand, the $^{3}He/^{4}He$ signature shows significant variations in the central and northern parts of the CVZ segment, which is reflected in FI from other volcanoes as well as most fumarole gases within the $^{3}He/^{4}He$ MORB range, as also observed in several other arc volcanoes (Rizzo et al., 2022 and references therein). This implies that the variable sediment input from the subducting slab (highlighted by U/Th; Fig. 9) and the extent of mantle melting do not have a significant effect on Rc/Ra, which is instead influenced by the local crustal characteristics (structural geology and rheological heterogeneities;

Roulleau et al., 2018; Veloso et al., 2021; Tardani et al., 2016, 2021) as well as the magma ascent history involving ^{4}He addition from basement rocks.

6. Conceptual model: a geothermal system connected to a source of magmatic fluid recharge

The gas samples at Tolhuaca volcano, including those from wells and the fully automated gas measurements at the surface, provide a comprehensive gas-mixture C-O-H-S chemical model of the Tolhuaca Geothermal System (Fig. 2, 4). The MI approach enables us to reconstruct the vertical profile of the magma vapor zone (e.g. Los Humeros, Mexico; Créon et al., 2018) (Fig. 4, 7), while bulk FI analyses for noble gases (Fig. 5) provide a valuable means of recovering fluid chemistry information for individual magmatic geothermal systems, giving insight into potential conditions for hydrothermal ore deposit formation (Moon, 1991; Blamey, 2012). Both types of inclusion (MI and FI) are shown to be powerful tools for interpreting the structure of magma-related high-enthalpy geothermal systems (Scott et al., 2014, 2015). For the first time, naturally preserved MI have been used to estimate the melt volatile contents of Tolhuaca glacial to post-glacial volcanic vents (Fig. 4), together with the isotopic signature of preserved fluids in rock samples using FI entrapped in olivine phenocrysts (Fig. 5). Our conceptual model is illustrated in figure 8.

The hydrothermal fields are divided up in terms of gas composition up to the present day (Fig. 1c; 6, 8), combining degassing process with magmatic gases (high Rc/Ra, CO_2/H_2S; CO_2/CH_4) together with hot fluid upward flow of meteoric water and little direct contact with the atmosphere (high CO_2/Ar). Local structures (Sánchez-Alfaro et al., 2013; Pérez-Flores et al., 2017) and the impermeable cap layer described by Melosh et al. (2010, 2012) facilitate the mixing of meteoric water with hot water circulating through the permeable zone in the vicinity of the amphitheater collapse fractures (at the site of the exploration camp). Combining our new surface and well dataset for gases with the hydrothermal minerals identified in the literature (Moore, 2009; Sánchez-Alfaro et al., 2016; Tardani et al., 2017), we calculated geothermometric gas values of 250-300°C, which are characteristic of active volcanic geothermal systems (>250°C for sub-greenschist facies of metamorphism). Paragenetic calcite, pyrite and pyrrhotite (and other sulfides, Tardani et al., 2017) are found at >670 m, which we infer to have precipitated when hot fluids containing carbon and H_2S reacted with oxidized magmatic gases entering the geothermal system (Arnórsson et al., 2010). Lower down the NW flanks of Tolhuaca H_2S-rich+CO_2-poor fluids are contaminated by air (low CO_2/Ar), but the lower ratio of CO_2/H_2S as well as CO_2/CH_4 now confirm a mixed-air gas composition away from the magmatic source. In the northern sector and at the peripheral fumaroles, the cooler water from the surface as well as fluid from the deeper hydrothermal system may dissolve

larger quantities of CO_2 from the gases that are transported through the crust or alternatively the gas content of H_2S does not vary upon dissolution processes when surface and deep-water currents mix (e.g. Termas de Pemehue, Avellano, Agua de la Vaca; Tardani et al., 2016).

The MI compositions and geothermobarometric conditions used in this study helped to define the depth zone for volatile separation and oxidation (between 1.1 and 1.8 km), specifically at a few hundred meters below the boiling depth (0.95 km; Sánchez-Alfaro et al., 2016) and concorded with upper limit of deep hydrothermal reservoir estimated with MT (Pavez et al., 2022) (Fig. 5, 7, 8). The Tolhuaca mafic magma could contain a maximum volatile content of 4.0 wt% H_2O (2500 ppm CO_2; >500 ppm S), which would derive from new gases from an oversaturated reduced melt (redox NNO = 0.5–1.5; T = 1163 °C at >593 bars; 2.50 km) in equilibrium with 22% xmol H_2O to produce a mixture of gases. The hypothetical gas mixture modelled at the surface from degassed MI (<20 m) has CO_2/S_t gas ratios of 0.3 to 34.5 and > 85 mol.% H_2O (Fig. 7ab), similar to monitored regional SVZ hydrothermal fields and typical of geothermal fluids (>90% water component; Nicholson, 1993), which fits theoretical Solex and D-Compress degassing models (Whitam et al., 2012; Burgisser et al., 2015). If the fluids operate directly below the Cono Canción volcanic vent, then a vertical circulation of magma in equilibrium with magmatic fluids (redox NNO = 2.0–3.0; T = 980 °C) would pass through a plumbing system at depths of 0.9–3.3 km under saturation conditions (according to solubility models; Fig. 5, 7). Our conceptual degassing model (Fig. 7ab; Fig. 8) proposes a magma which (1) exsolves CO_2 and oxidizes sulfur, then (2) releases water as vapor at 300-500 bars (1.08–1.8 km), before (3) it meets and mixes with the hydrothermal reservoir (<1.5 km), and finally (4) hot gases and thermal diffusion enhance boiling at the reported depth of 0.95 km (> 1.0 km interpreted to be shallow reservoir in Pavez et al. (2022), as identified from studies at exploration wells (Melosh et al., 2012).

We show that petrogenetic information needs to be incorporated in order to understand the full system from mantle to surface geothermal fields (Fig. 3, S2, 5, 9). The high bulk rock Sr/Y, K_2O wt.% in MI, petrological evidence of silicate melt mixing (reverse Fo% and Mg# zoning) and low equilibrium temperatures, all demonstrate the effects of local crustal interaction on an individual volcanic center; Cono Canción andesitic-to dacitic magmas (Fig. S2, 8) in this study demonstrate all of these magma-mixing-contamination factors and provide evidence for crustal incorporation of ^4He into magmatic fluids transported within the Tolhuaca plumbing system. The crustal ^4He addition to hydrothermal fluids also demonstrates that the mantle fluid signature at Tolhuaca decreases with transport distance (Dobson et al., 2013; Tardani et al., 2016). The bulk rock composition contains a characteristic slab-fluid signature from the mantle (high Ba/Nb, Th/La, etc.), but given the similar distance to slab and location with respect to Tolhuaca Fissural and other MECs to the SW of Tolhuaca, this could not explain the lack

of sediment-fluid signature (high U/Th) that marks the basaltic-to basaltic andesites MEC around this stratovolcano (e.g. Cono Caracol); the pattern here over the length of the ~3 km fracture is not representative of a typical evolved magma series (basaltic to rhyolitic) linked to ATF structures (Cembrano and Lara, 2009) or crustal contamination of the gases (Tardani et al., 2016). The noble gases in FI from olivine crystals with heterogenous compositions (maximum Fo_{82}) exhibit a local peak in $^{3}He/^{4}He$ ratio of 8.20 Ra, in the region, representing the most MORB-like magmatic source in the C-SVZ (Tardani et al., 2016; Roulleau et al., 2016), therefore Tolhuaca magmas and associated fluids succeed in passing through the continental crust by means of the WNW trending fractures that cross this sector of the volcanic system with little modification to their primary composition.

Credit Authorship contribution statement

Philippe Robidoux: Conceptualization, Resources, Methodology, Visualization, Data acquisition, Data curation, Validation, Investigation, Writing - original draft, Writing - review and editing, Supervision, Funding acquisition

Daniele Tardani: Validation, Resources, Methodology, Data curation, Investigation, Writing -review and editing

Pablo Sánchez-Alfaro: Validation, Resources, Methodology, Investigation, Writing -review and editing

Marco Liuzzo: Resources, Data acquisition, Methodology, Data curation, Writing -review and editing

Diego Morata: Methodology, Resources, Investigation, Visualization, Writing - review and editing, Funding acquisition

Estelle F. Rose-Koga: Resources, Data acquisition, Methodology, Data curation, Writing -review and editing

Yves Moussallam: Data acquisition, Methodology, Data curation, Writing -review and editing

Franco Tassi: Data acquisition, Methodology, Data curation, Writing -review and editing

Pamela Pérez-Flores: Methodology, Writing - review and editing

Fausto Grassa: Methodology, Writing - review and editing

Vincenzo Francofonte: Methodology, Data curation

Uncited Reference

Declaration of Competing Interest

The authors declare that they have no known competing financial interests or personal relationships that could have appeared to influence the work reported in this paper.

Data availability

The data supporting the findings of this study are available within the article.

Acknowledgements

This work is part of ANID, Fondecyt Iniciacion No 11190846 project of Philippe Robidoux (2019-2022), Fondecyt Iniciacion No 11220777 project of Daniele Tardani and Fondap No ACE210005, Centro de Excelencia en Geotermia de Los Andes (CEGA) managed by Diego Morata. We are grateful to Dra Manuela Nazzari and Dir. Piergiorgio Scarlato for providing access to electron microprobe EMPA at Istituto Nazionale di Geofisica e Vulcanologia Sezione di Roma 1, HP-HT Lab. of Experimental Volcanology and Geophysic. The measurements were also supported by Elisabetta Del Bello and Alessio Pontiselli (INGV-Roma) through participation at the TransNational Access (TNA) in the framework of the EXCITE (Horizon 2020) research infrastructure. Special thanks are sent for Dr. Andrea Rizzo and staff from INGV-Palermo for analysis on noble gases; Mariano Tantillo and Mariagrazia Misseri helped mineral preparation with their assistance during noble gases isotope analysis. Special thanks for the staff who helped on Multigas preparation during the years 2019-2021 (Sergio Gurrieri, Giovanni Giuffrida). Special thanks to Veronica Rodriguez (CEGA) for laboratory support on gas sampling and preparation. We acknowledge the long-term support of Carolina Wechsler P. and Alberto Espinoza P., both geologists from Transmark to kindly help coordinate field sampling and furnishing resourceful discussions. We adress special acknowledgements for Universidad Mayor, Escuela de Geología as Universidad de Chile (Depart. Geología) students for active participation in the field trips. ER-K, YM and PR deeply thank Nordine Bouden and Johan Villeneuve for their flawless support with the SIMS measurements and for the access to the Nancy preparation lab when we needed to perform “surgery” on one of the indium mount.

References

Figure1

Click here to access/download;Figure;Fig1.jpg

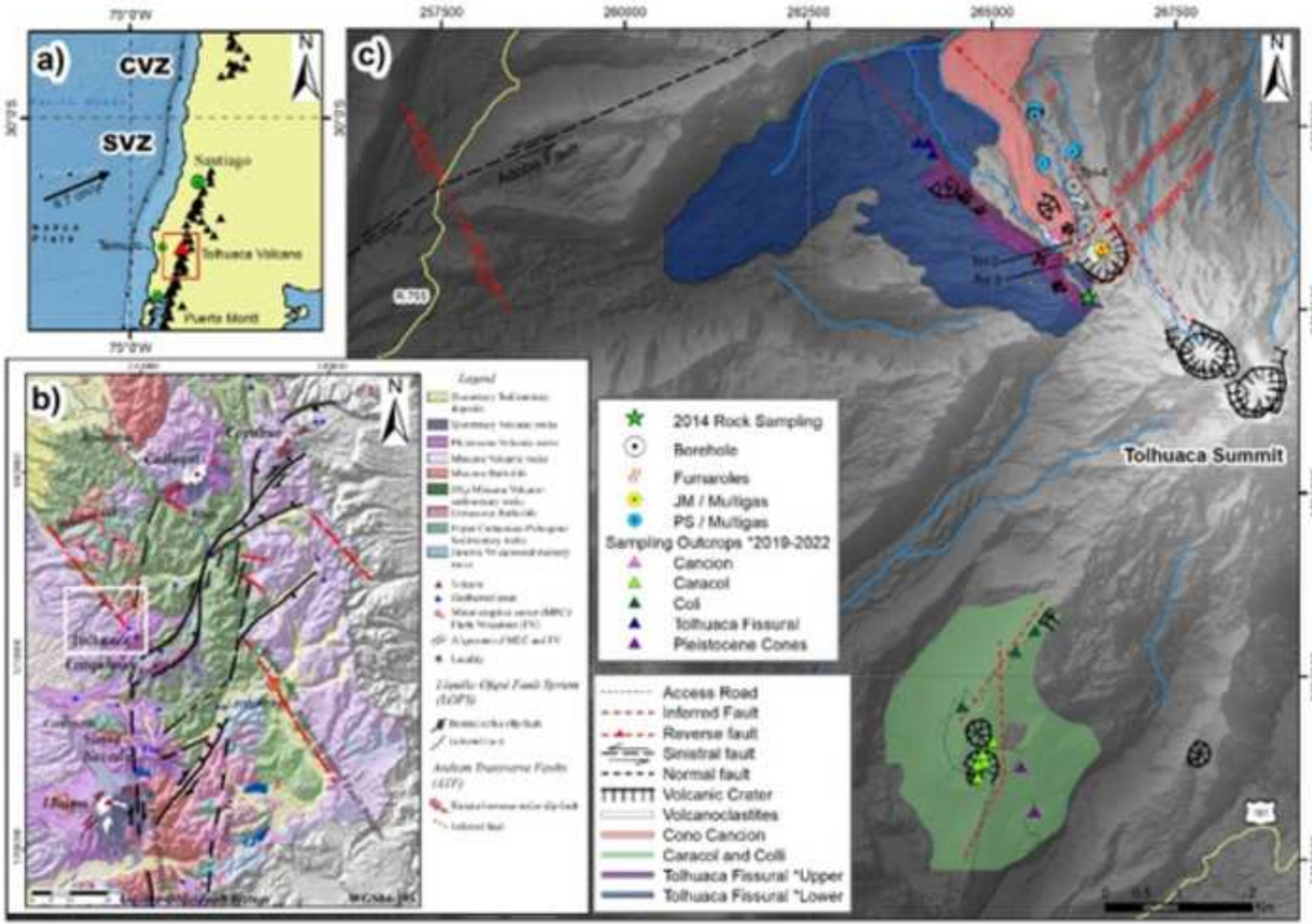

Figure2

Click here to access/download;Figure;Fig2.jpg

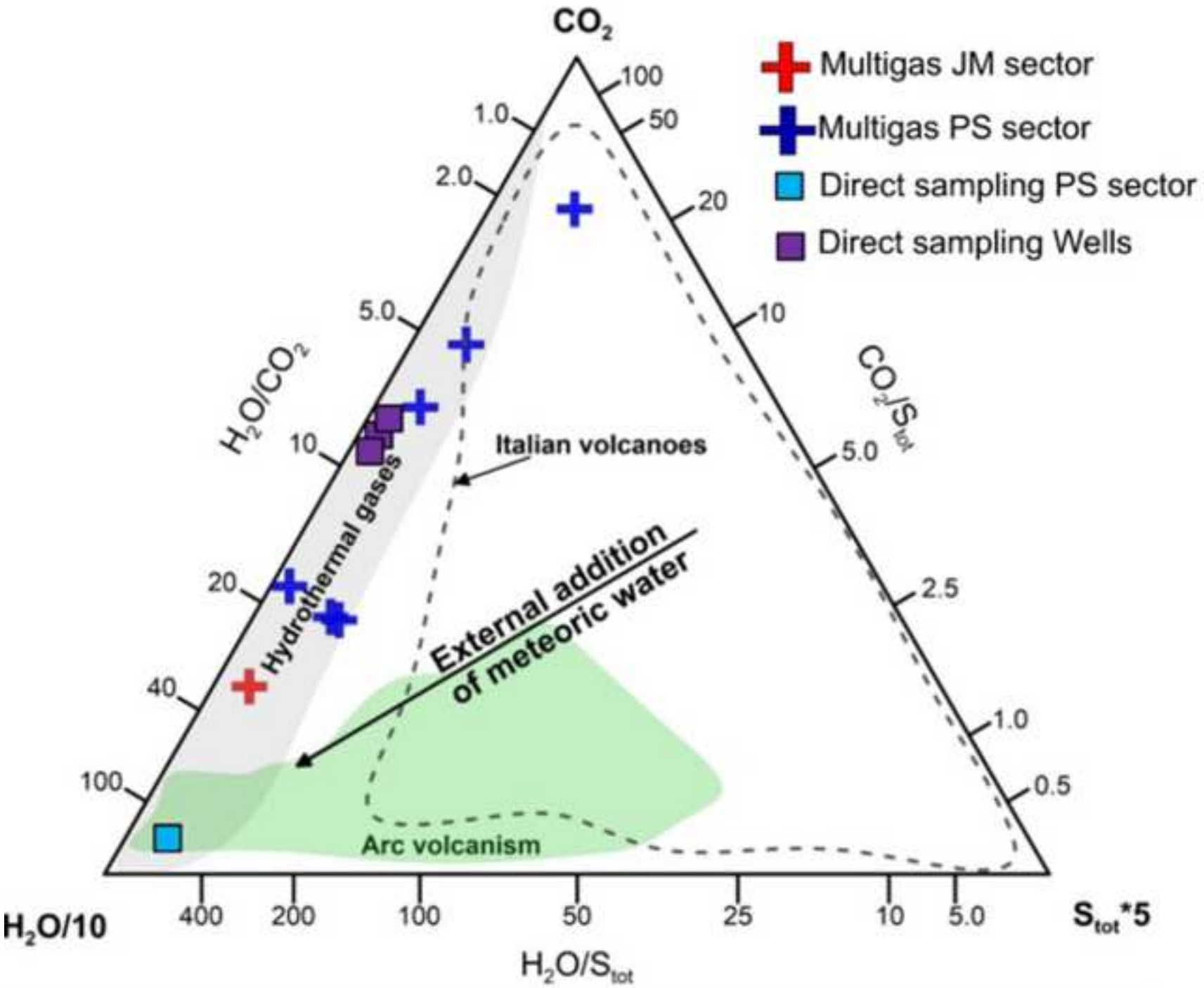

Figure3

Click here to access/download;Figure;Fig3.jpg

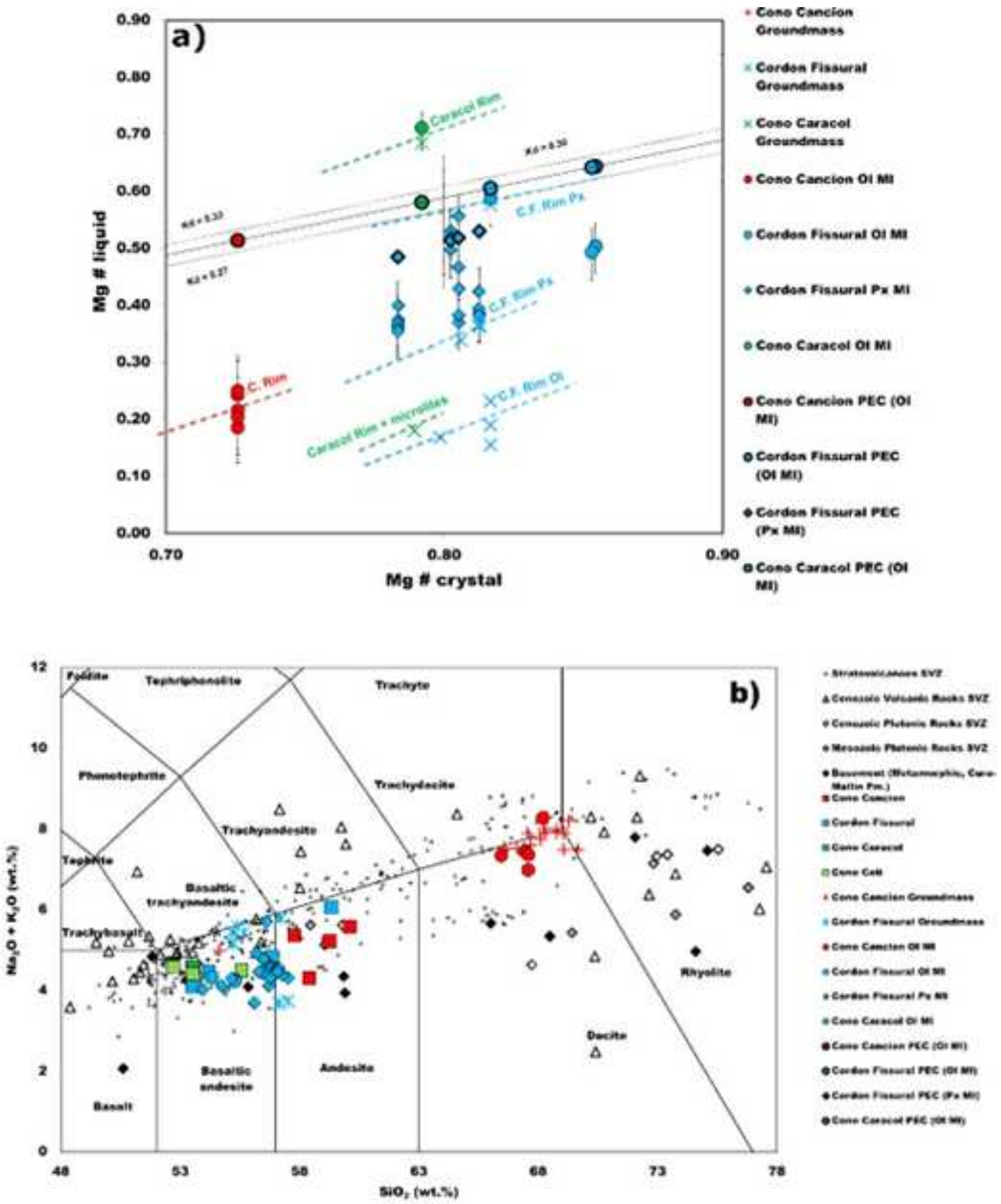

Figure4

Click here to access/download;Figure;Fig4.jpg

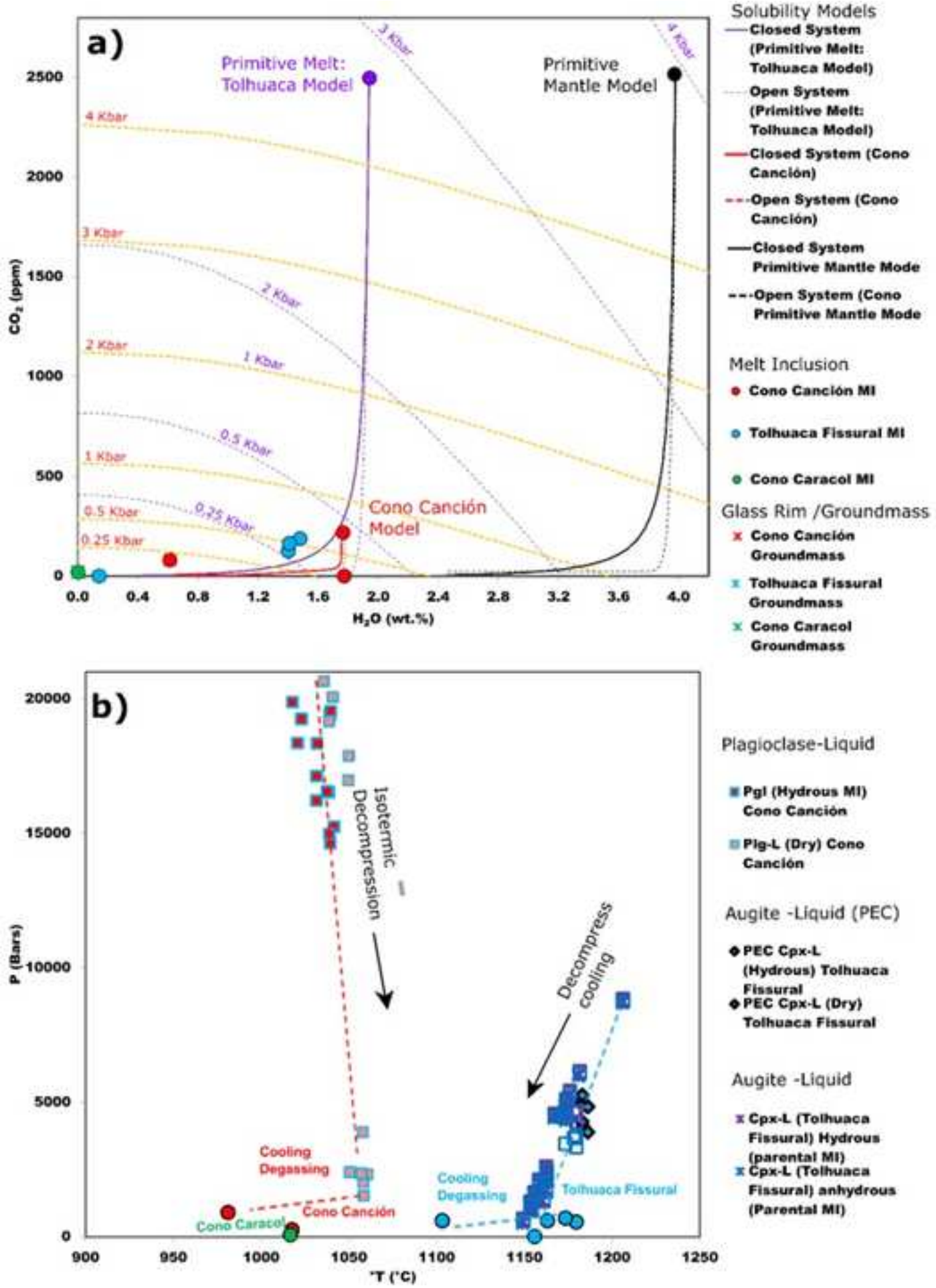

Figure5

Click here to access/download;Figure;Fig5.jpg

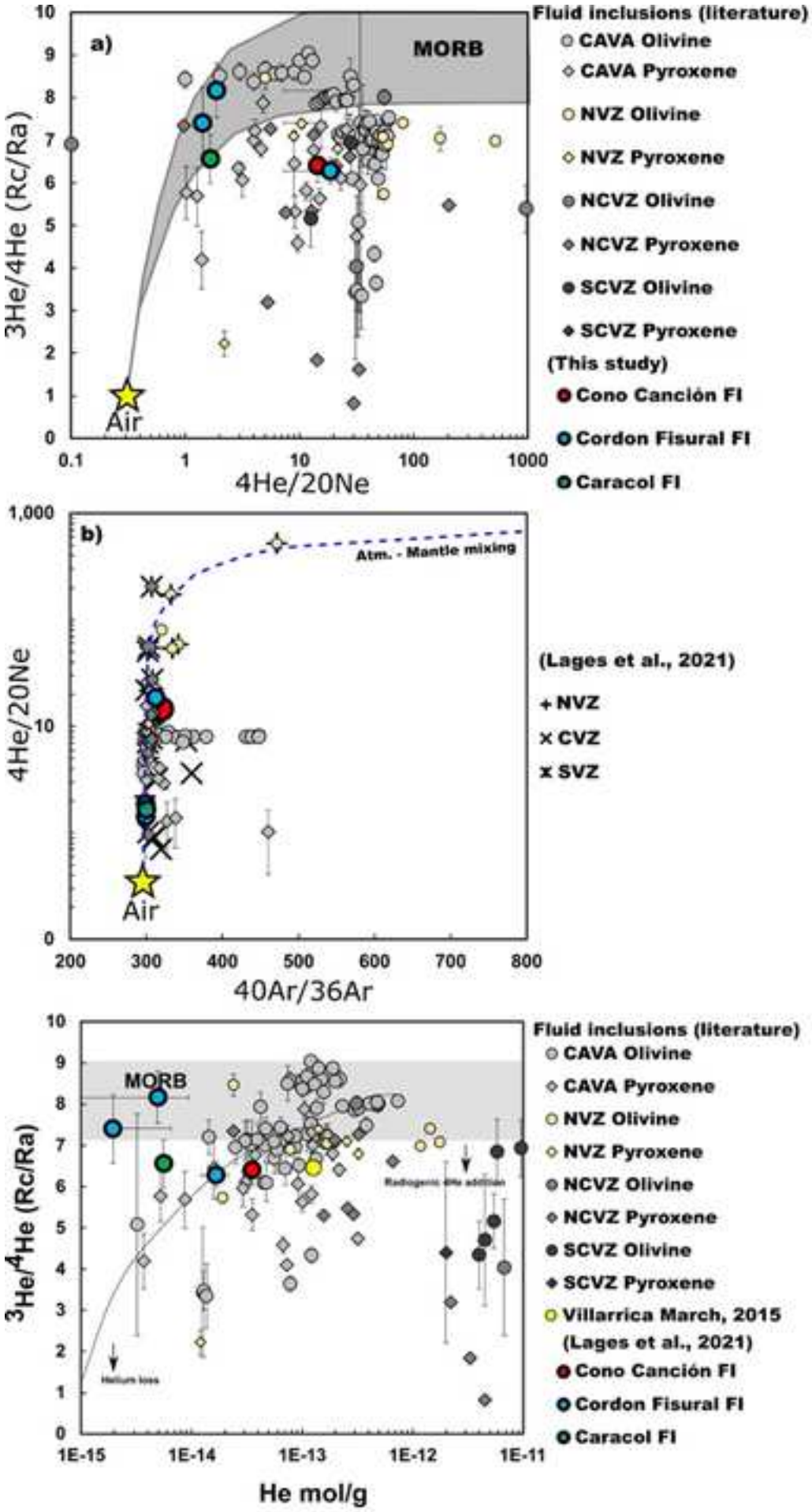

Figure6

Click here to access/download;Figure;Fig6.jpg

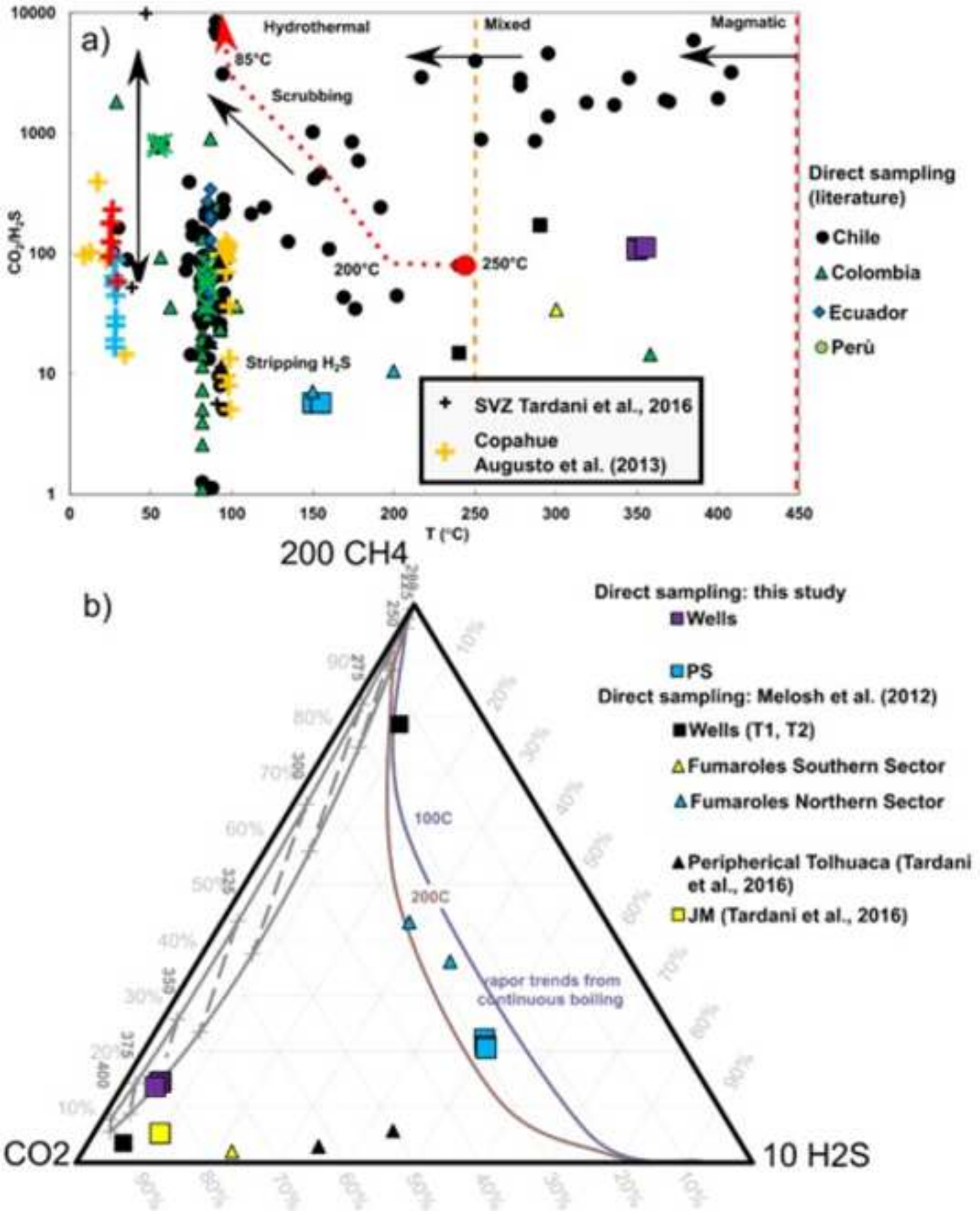

Figure7

Click here to access/download;Figure;Fig7.jpg

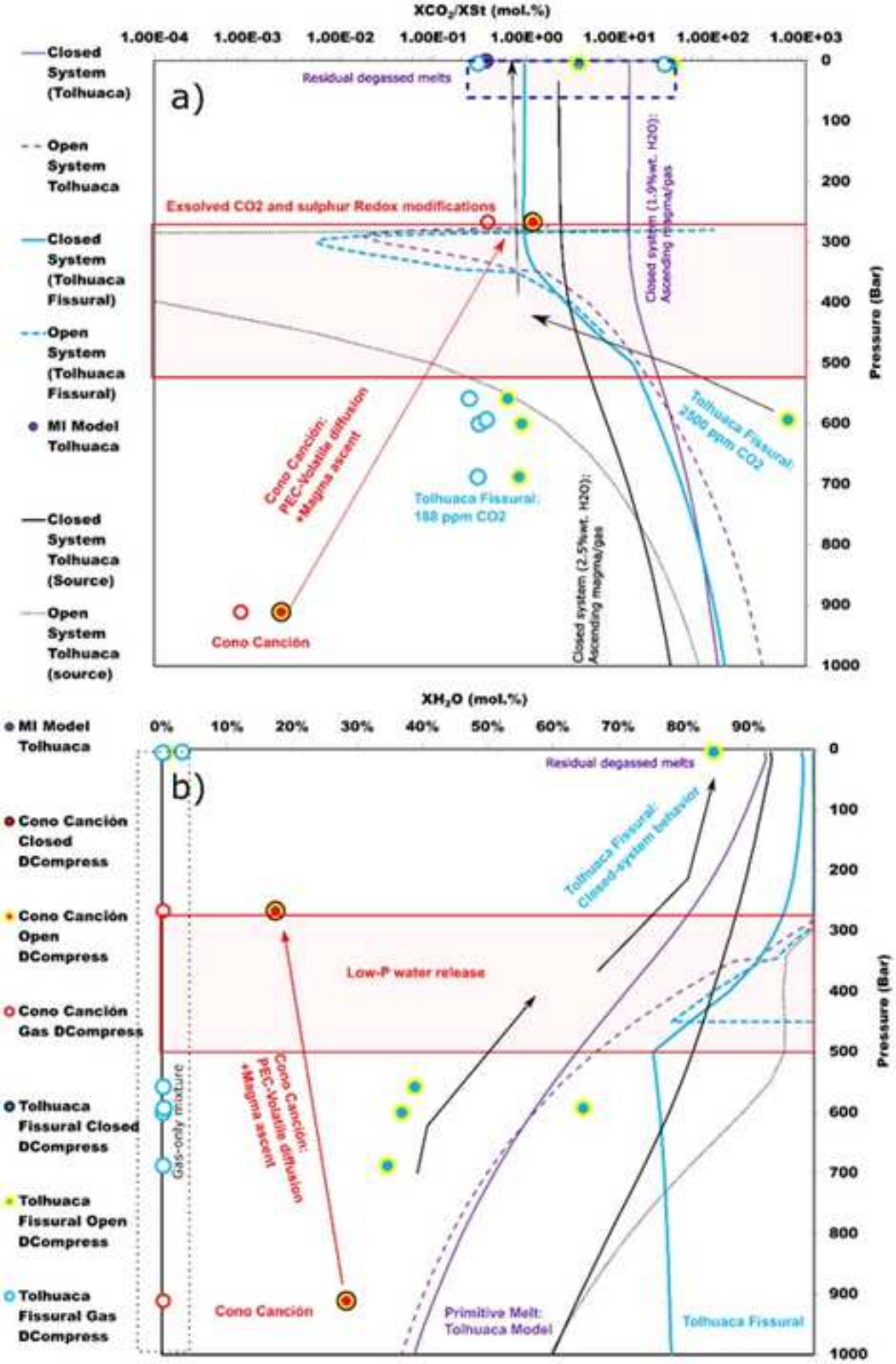

Figure8

Click here to access/download;Figure;Fig8.jpg

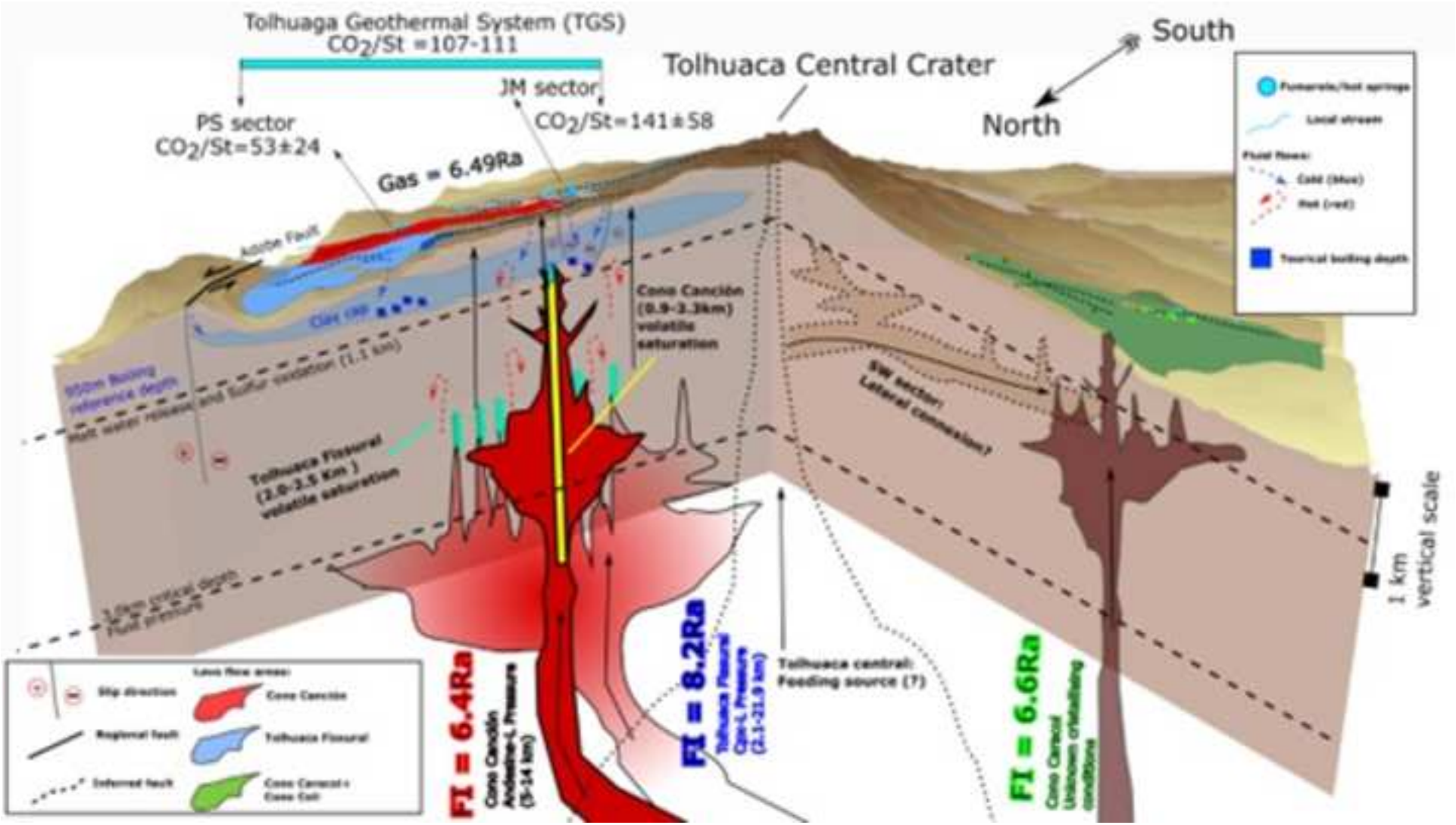

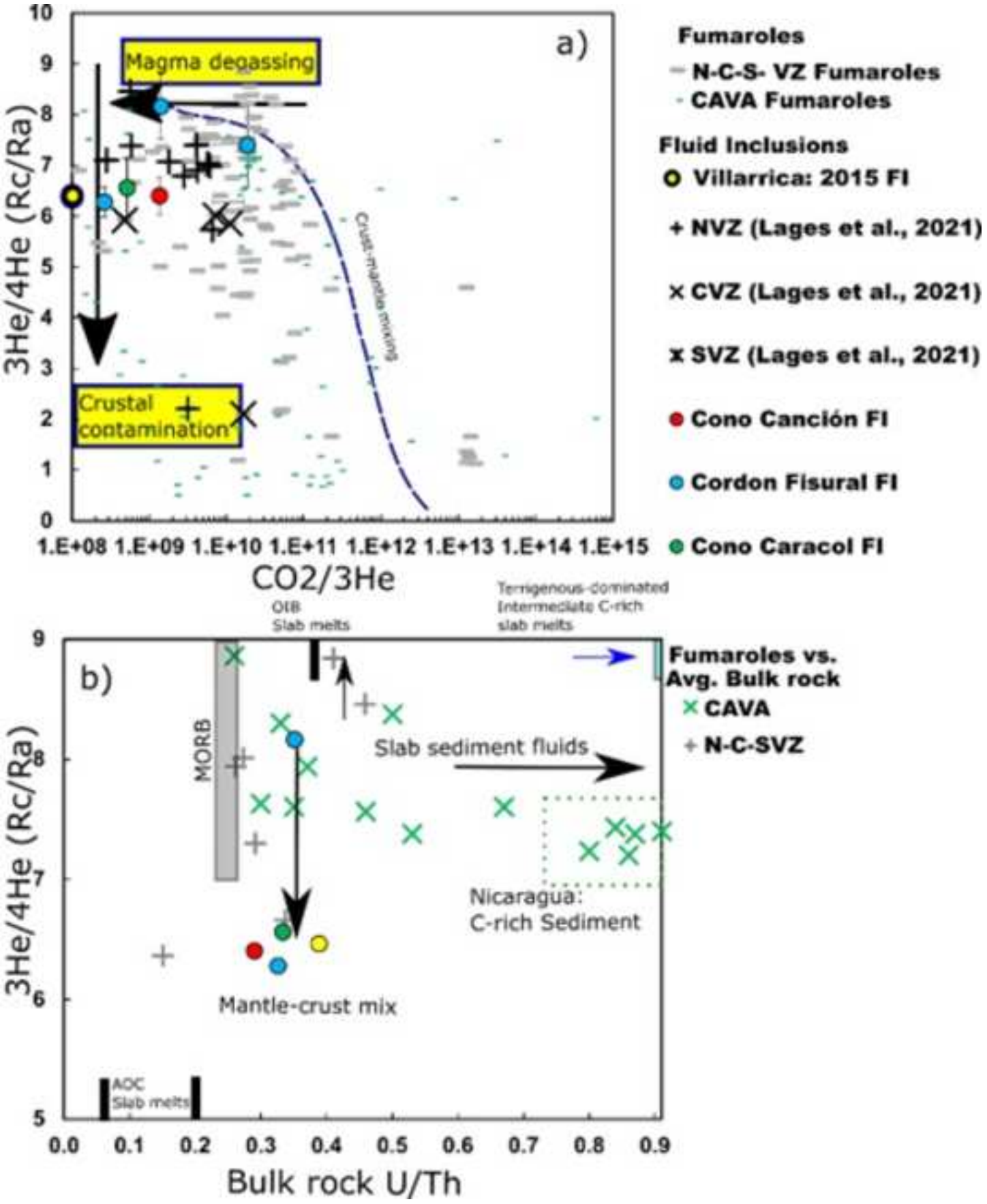

Table 1. MultiGAS Derived Molar Ratios

Discharge Site	Typology	Time	CO_2/H_2S	H_2O/CO_2	H_2O/H_2S
Sector Jaime Muro					
JM3	Fumarole	11/26/2021 15:13	94.9	3.1	436
Sector Pablo Sola					
PS1	Fumarole	12/9/2021 16:50	44.9	1.2	354
PS2	Fumarole	12/9/2021 16:53	58.3	6.6	1230
PS5	Bubbling hot spring	12/9/2022 18:50	19.2	19.2	1503
PS5	Bubbling hot spring	11/9/2021 15:50	16.7	19.2	1503
PS11	Bubbling hot spring	12/9/2022 19:37	55.0	4.5	417
PS17	Bubbling hot spring/deep rock	12/9/2022 20:03	88.1	17.8	748

Dates are formatted as day/month/year.

Table 2: Chemical composition of Tolhuaca fumarole, bubbling gas and water-dissolved gas samples

Well sample n°	CO_2	H_2S	N_2	CH_4	Ar	O_2
	ppm	ppm	ppm	ppm	ppm	ppm
Tolhuaca 1	980086	8754	5487	625	34	61
Tolhuaca 2	978901	9111	5698	555	39	55
Tolhuaca 3	980290	8647	5574	512	35	68

Fumarole sample n°	CO_2	H_2S	N_2	CH_4	Ar	O_2
	%	%	%	%	%	%
PB1	81.597	14.083	0.718	0.317	0.019	0.023
PB2	81.979	14.149	0.582	0.298	0.017	0.005
PB3	82.065	14.164	0.564	0.290	0.017	0.013

H_2	He	CO	
ppm	ppm	ppm	
4875	5.6	23.56	111.9586795
5564	4.4	20.84	107.4417122
4798	4.8	21.49	113.3676709

H_2	He	Xgas %	
%	ppm	%	
3.242	8	0.61	5.794015659
2.969	6	0.61	5.794015659
2.887	7	0.61	5.794015659

Table 3 (Editable version)

Click here to access/download;Table (Editable version);Table3.xlsx

Table 3: Chemical compositions of bulk rocks

Sample	CC1	CC1	N12CC	CC12022	CAO4-A	CA02A	COO1B	CO03	COO2	FI1A	TO1B	NV18
Order	Cono Canción				Caracol		Cono Colli			Tolhuaca: Fisural 1	Tolhuaca: Fisural 2	Tolhuaca: Early Fisural 1
Description	Porphyric texture, variable dimensions, grey-dark, large vesicular			See "CC1"	Vitrophyric basalt scoriae	Porphyric texture, banded dark glassy groundmass, parrallel vesicules	Microporphyric, vitrophyric, vesicular texture scories	Porphyric texture		Vesicular-porphyric pyroclast of lapilli-size found in scoriaceous breccia	Porphyric texture, grey color, high density vesicules with microcrystals	Porphyric bomb, microcristalline, almost no vesicules
Rock Name	Scoriae-bomb			Block-bomb	Vesicular scoriae	Pahoehoe bomb scoriae	Scoriae	Porphyric lava		Vesicular scoriae	Scoria-Breccia lava	Block
SiO_2 (wt.%)	56.79	57.97	59.26	54.27	51.86	52.47	52.4	51.72	55.16	58.52	52.38	55.29
Al_2O_3	17.09	16.9	15.75	18.01	18.33	18.22	18.36	19.11	18.37	16.58	17.92	16.83
FeO		4.6				1.7						6.2
Fe_2O_3	7.41	2.04			10.61	8.46	10.76	8.74	8.51	8.82	9.96	1.28
MnO	0.12	0.12	0.119	0.105	0.19	0.18	0.19	0.15	0.14	0.16	0.17	0.14
MgO	4.12	3.58	3.72	3	3.77	3.61	3.85	3.5	3.2	2.09	3.97	4.01
CaO	6.47	6.47	6.03	5.34	7.77	7.35	7.91	7.8	8.09	4.95	7.46	7.55
Na_2O	3.61	3.53	3.57	2.81	4.01	3.81	4.04	3.65	3.69	4.58	3.55	3.49
K_2O	1.66	1.58	1.93	1.19	0.53	0.67	0.52	0.61	0.77	1.4	0.93	1.21
TiO_2	0.84	0.87	0.796	0.879	1.22	1.29	1.23	1.15	1.13	1.28	1.28	1.04
P_2O_5	0.16	0.16	0.16	0.15	0.16	0.21	0.19	0.19	0.2	0.26	0.24	0.25
Cr_2O_3	0.014	n.d.	n.d.	n.d.	n.d.	n.d.	n.d.	0.003	n.d.	n.d.	0.004	n.d.
LOI	1.5	1.3	-0.06	6.21	1.3	2.51	0.3	3.2	1.04	1.2	1.9	0.44
Sum	99.9	99.62	98.52	99.13	99.88	100.7	99.88	99.9	100.3	99.92	99.87	98.42
Fe_2O_3(T)	-	7.16	7.26	7.18	-	10.35	-	-	8.52	-	-	8.17
H_20^+	n.d.	1.2	n.d.	n.d.	n.d.	1.8	n.d.	n.d.	0.6	n.d.	n.d.	0.7
Cs (ppm)	5.55	0.21	5.5	-	0.04	1.28	0.04	0.12	0.94	0.38	0.72	3.6
Rb	53.2	1	48	-	0.3	13	0.3	0.6	12.8	1.8	1.5	34.5
Ba	343	18.9	345	-	13.8	231	19.1	22.5	256	37.2	36.8	328
Th	6.8	0.6	6.9	-	0.3	1.5	0.3	1.2	1.4	3.4	2.9	4.3
U	2.1	0.17	2	-	0.05	0.5	0.06	0.34	0.6	0.41	0.79	1.4
Ta	0.1	-	0.2	-	-	0.1	-	-	0.1	-	-	0.1
Nb	0.1	0.02	3	-	0.12	0.2	0.04	0.06	1.2	0.03	0.29	0.1
K	13116.054	13780.158	9086.568162	-	4399.689	5561.871	4316.676	5063.79	6392	11621.82	7720.209	10044.573
La	12.9	1.6	13.5	-	3.3	8.4	2.2	9.8	7.4	11.6	10	13
Ce	31.9	4	29.6	-	7.8	22.1	5.1	16.5	18.1	30.9	22.7	32.8
Pb	15.8	-	14	-	-	7.9	-	-	8.2	-	-	13.5
Pr	4	0.51	3.91	-	1.17	3	0.72	2.97	2.7	4.24	3.24	4.2
Sr	398	89.1	416	-	144.4	510	146.9	118.8	489	26.9	69.8	448
Nd	18.1	2.43	17	-	5.58	14.7	3.56	13.5	12.8	19.28	14.64	19.8
Hf	-	0.21	4.8	-	0.2	-	0.22	0.12	-	0.38	0.62	-
Zr	119	7.9	171	-	7.1	83	7.2	5.1	96	9.8	25.1	105
Sm	4.2	0.56	4.2	-	1.27	3.9	0.89	2.41	3.1	4.09	2.85	5
Eu	1.02	0.14	1	-	0.32	1.27	0.28	0.82	0.97	0.36	0.35	1.18
Ti	5215.65	5035.8	5668.836854	-	7313.9	7733.55	7373.85	6894.25	6774.35	7673.6	7673.6	6234.8
Dy	4	0.48	4	-	1.15	4	0.86	2.19	3.1	3.24	2.11	4.6
Y	22.3	2.15	22	-	5.49	21.5	4.24	13.35	16.2	16.15	10.06	25.1
Yb	2.4	0.22	2.3	-	0.57	2.3	0.45	1.02	1.8	1.6	0.8	2.7
Lu	0.3	0.04	0.36	-	0.08	0.3	0.07	0.14	0.3	0.21	0.11	0.4
Ba/Nb	3430	945	115	n.d.	115	1155	478	375	213	1240	127	3280
Zr/Nb	1190	395	57	n.d.	59	415	180	85	80	327	87	1050
Sr/Y	17.8	41.4	18.9	n.d.	26.3	23.7	34.6	8.9	30.2	1.7	6.9	17.8
La/Yb	5.4	7.3	5.9	n.d.	5.8	3.7	4.9	9.6	4.1	7.3	12.5	4.8
Sr/La	30.9	55.7	30.8	n.d.	43.8	60.7	66.8	12.1	66.1	2.3	7.0	34.5
Ba/La	26.6	11.8	25.6	n.d.	4.2	27.5	8.7	2.3	34.6	3.2	3.7	25.2
Th/La	0.5	0.4	0.5	n.d.	0.1	0.2	0.1	0.1	0.2	0.3	0.3	0.3
U/La	0.2	0.1	0.1	n.d.	0.0	0.1	0.0	0.0	0.1	0.0	0.1	0.1
U/Th	0.3	0.3	0.3	n.d.	0.2	0.3	0.2	0.3	0.4	0.1	0.3	0.3
Sr/Eu	390	636	416	n.d.	451	402	525	145	504	75	199	380
Eu/EU*	0.7	0.7	0.7	n.d.	0.7	1.0	0.9	1.0	1.0	0.3	0.4	0.7

TO1A	**tol-01**
Tolhuaca: Fisural 1	
Vesicular-porphyric pyroclast of lapilli-size found in scoriaceous breccia	
Vesicular scoriae	
52.15	53.56
18.27	17.4
6.1	
3.4	
0.17	0.146
3.66	6.35
6.56	8.17
3.24	3.22
1.06	0.88
1.35	1.009
0.28	0.21
n.d.	n.d.
3.75	0.12
100.7	100.2
10.18	9.14
3.6	n.d.
1.78	-
24	-
290	-
3.7	-
1.3	-
0.1	-
0.1	-
8799.378	-
10.1	-
26.6	-
13.7	-
3.5	-
395	-
16.7	-
-	-
118	-
4.9	-
1.29	-
8093.25	-
4.4	-
23.4	-
2.8	-
0.4	-
2900	n.d.
1180	n.d.
16.9	n.d.
3.6	n.d.
39.1	n.d.
28.7	n.d.
0.4	n.d.
0.1	n.d.
0.4	n.d.
306	n.d.
0.8	n.d.

Table 4 (Editable version)

Click here to access/download;Table (Editable version);Table4.xlsx

Inclusion Phenocryst	NExtra_CC1m65r	NExtra_CC1l1c7v1	NExtra_CC1l1c7v2
Stratigraphy	Cono Canción	Cono Canción	Cono Canción
Phenocryst chemistry (Fo)	23.08	72.58	72.58
SiO_2, *wt.%*		70.38	69.21
TiO_2		1.19	0.98
Al_2O_3		15.65	16.87
FeO*		0.61	0.54
MnO		0.03	0.00
MgO		0.36	0.32
CaO		3.48	3.98
Na_2O		4.81	4.69
K_2O		3.19	3.18
P_2O_5		0.30	0.23
TOT		100	100
T (°C) by KP	981	1057	1029
H_2O (*wt.%*) nSIMS	1.77		
CO2 (*µg/g*) nSIMS	0		
S (µg/g) EMPA	49		
Cl (µg/g) EMPA	4082		
F (µg/g) EMPA	449		
H_2O (*wt.%*) mFTIR			
CO2 (*µg/g*) mFTIR			
Sat. Press. (Bar)	910		
Err. Sat. Press. (Bar)			
°T-dependeant Buffer fO_2	-10.48		
KD Original	-	0.104	0.086
% Olivine added	-	5.21	5.15
% Augite added	-	-	-

NExtra_CC1l1c7v3	NExtra_CC1l1c7v5	NExtra_CC1l1c7v6	**Inclusion Phenocryst**
Cono Canción	Cono Canción	Cono Canción	**Stratigraphy**
72.58	72.58	72.58	**Phenocryst chemistry (Fo)**
70.45	69.98	70.87	**SiO_2,** *wt.%*
1.19	1.11	1.27	**TiO_2**
15.90	16.38	15.18	**Al_2O_3**
0.46	0.50	0.55	**FeO***
0.00	0.09	0.02	**MnO**
0.27	0.30	0.32	**MgO**
3.60	3.92	2.70	**CaO**
4.81	4.89	4.22	**Na_2O**
3.09	2.53	4.60	**K_2O**
0.23	0.30	0.27	**P_2O_5**
100	100	100	**TOT**
1026	1018	1026	**T (°C) by KP**
	0.61		**H_2O (*wt.%*) nSIMS**
	80		**CO2 (*µg/g*) nSIMS**
	6		**S (µg/g) EMPA**
	1259		**Cl (µg/g) EMPA**
	508		**F (µg/g) EMPA**
			H_2O (*wt.%*) mFTIR
			CO2 (*µg/g*) mFTIR
	245		**Sat. Press. (Bar)**
	46		**Err. Sat. Press. (Bar)**
	-9.95		**°T-dependeant Buffer fO_2**
0.086	0.097	0.125	**KD Original**
5.13	4.39	4.6	**% Olivine added**
-	-	-	**% Augite added**

NExtra_to1a29_miac	NExtra_to1a29_miar	NExtra_to1a29_mibc	NExtra_to1a29_mibr	NExtra_to1a104v1
Tolhuaca Fissural	Tolhuaca Fissural	Tolhuaca Fissural	Tolhuaca Fissural	Tolhuaca Fissural
80.23	80.23	80.23	80.23	78.33
54.78	54.63	53.84	54.90	
1.20	1.20	1.29	1.22	
15.45	15.23	15.27	14.91	
9.26	9.60	9.84	9.57	
0.16	0.13	0.14	0.13	
5.49	5.68	5.83	5.67	
9.37	9.34	9.73	9.21	
3.14	3.21	3.02	3.29	
0.80	0.74	0.80	0.69	
0.32	0.17	0.20	0.32	
100	100	100	100	
1180	1178	1180	1174	1154
1.40			1.48	
126			188	
471			497	
377			397	
305			318	
558			697	
116			143	
-7.78			-7.85	
0.245	0.236	0.230	0.215	-
-	-	-	-	-
0.0287	0.0472	0.0601	0.0888	-

NExtra_to1a104v2	**Inclusion Phenocryst**	NExtra_to1a104v3	NExtra_to1a32_mic	NExtra_to1a32_mir
Tolhuaca Fissural	**Stratigraphy**	Tolhuaca Fissural	Tolhuaca Fissural	Tolhuaca Fissural
78.33	**Phenocryst chemistry (Fo)**	78.33	85.44	85.30
	SiO_2, *wt.%*		55.38	55.54
	TiO_2		1.09	1.36
	Al_2O_3		15.67	15.50
	FeO*		7.48	7.18
	MnO		0.14	0.15
	MgO		7.47	7.12
	CaO		8.40	8.79
	Na_2O		3.32	3.35
	K_2O		0.79	0.76
	P_2O_5		0.27	0.25
	TOT		100	100
1159	**T (°C) by KP**	1156	1103	1100
	H_2O (*wt.%*) nSIMS	0.14	1.41	
	CO2 (*µg/g*) nSIMS	0	165	
	S (µg/g) EMPA	9	467	
	Cl (µg/g) EMPA	385	398	
	F (µg/g) EMPA	392	321	
	H_2O (*wt.%*) mFTIR			
	CO2 (*µg/g*) mFTIR			
	Sat. Press. (Bar)	4.4	646	
	Err. Sat. Press. (Bar)		132	
	°T-dependeant Buffer fO_2	-8.09	-8.73	
-	**KD Original**	-	0.153	0.148
-	**% Olivine added**	-	-5.67	-4.71
-	**% Augite added**	-	-	-

PR2_to1a49Xr_v4	NExtra_tolb9mi	NExtra_ca0257_mi2	NExtra_ca02a23_mia
Tolhuaca Fissural	Tolhuaca Fissural	Cono Caracol	Cono Caracol
81.66	82.68	81.77	78.94
52.81	45.82	63.94	
0.09	0.94	0.51	
19.39	16.74	21.40	
8.51	11.46	0.13	
0.00	0.18	0.05	
7.25	10.12	0.11	
7.56	12.47	1.46	
3.75	1.28	9.00	
0.64	0.83	2.54	
0.00	0.15	0.87	
100	100	100	
1126	1163	1020	1017
	1.94		0.00
	2497		20
	143		0
	1095		6
	189		70
	3525		76.2
	790		22
	-7.88		-9.97
0.282	0.269	0.117	-
-31	-12.25	-0.63	-
-	-	-	-

Table 5 (Editable version)

Click here to access/download;Table (Editable version);Table5.xlsx

Inclusion	**Phenocryst**		PR1_cc1l8c8Xv2	PR1_cc1l8c8Xv3	PR1_cc1l8c8Xv4
Groundmass spot		Plagioclase-rim	Plagioclase-rim	Plagioclase-rim	Plagioclase-rim
Stratigraphy		Cono Cancion	Cono Cancion	Cono Cancion	Cono Cancion
SiO_2, *wt.%*		66.88	65.77	65.43	66.77
TiO_2		1.00	0.85	1.03	0.83
Al_2O_3		13.60	13.81	13.47	13.75
FeO*		4.94	4.20	4.97	3.96
MnO		0.08	0.05	0.13	0.08
MgO		0.53	0.38	0.58	0.47
CaO		2.27	2.74	2.32	2.34
Na_2O		4.91	4.14	4.08	4.47
K_2O		2.35	3.43	3.52	3.45
P_2O_5		0.27	0.25	0.29	0.27
NiO				0.02	
SO_3			0.10		0.01
TOT		96.82	95.73	95.84	96.40
H_2O (*wt.%*) nSIMS					
CO2 (*µg/g*) nSIMS					
S (µg/g) nSIMS					
Cl (µg/g) nSIMS					
F (µg/g) nSIMS					
S (µg/g) EMPA			396		40
Cl (µg/g) EMPA					
F (µg/g) EMPA					
Olivine-L °T (°C)					
Hygrometer H_2O (wt. %) *L		0.52	1.22	1.03	1.13
Hygrometer H_2O (wt. %) *L2		3.02	4.03	3.46	3.81
P(kbar)		16.3	18.5	17.8	19.2
°T(°C)		1034	1006	1009	1003
$KD_{(Ab-An)}$		0.24	0.25	0.24	0.24

PR1_cc1l8c8Xv5 Plagioclase-rim Cono Cancion	PR1_cc1l10c3Xv Oxide-rim Cono Cancion	**Inclusion Phenocryst Groundmass spot Stratigraphy**	PR1_cc1l10c3Xv Oxide-rim Cono Cancion	PR1_cc1l10c3Xv3 Oxide-rim Cono Cancion
66.38	66.25	**SiO_2,** *wt.%*	66.81	65.98
0.98	0.97	**TiO_2**	0.99	1.05
13.39	13.65	**Al_2O_3**	13.26	13.90
4.93	5.19	**FeO***	4.70	4.52
0.06	0.04	**MnO**		0.04
0.58	0.68	**MgO**	0.65	0.60
2.24	2.27	**CaO**	2.32	2.18
5.12	4.94	**Na_2O**	4.92	4.75
2.60	2.83	**K_2O**	2.72	3.24
0.24	0.27	**P_2O_5**	0.31	0.26
0.01		**NiO**	0.06	
0.03	0.03	**SO_3**		
96.56	97.13	**TOT**	96.73	96.51
		H_2O (*wt.%*) nSIMS		
		CO2 (*µg/g*) nSIMS		
		S (µg/g) nSIMS		
		Cl (µg/g) nSIMS		
		F (µg/g) nSIMS		
112	122	**S (µg/g) EMPA**		
		Cl (µg/g) EMPA		
		F (µg/g) EMPA		
		Olivine-L °T (°C)		
0.54		**Hygrometer H_2O (wt. %) *L**		
2.98		**Hygrometer H_2O (wt. %) *L2**		
17.2		**P(kbar)**		
1034		**°T(°C)**		
0.24		**$KD_{(Ab\text{-}An)}$**		

PR1_cc1l10c3Xv4	PR1_cc1l10c3Xv5	NExtra_CC1l1c7v1	NExtra_CC1l1c7v2	**Inclusion Phenocryst**
Oxide-rim	Oxide-rim	Olivine-rimivine-rim	Olivine-rimivine-rim	**Groundmass spot**
Cono Cancion	Cono Cancion	Cono Cancion	Cono Cancion	**Stratigraphy**
65.49	66.40	66.44	65.33	**SiO_2,** *wt.%*
0.94	0.96	1.09	0.90	**TiO_2**
13.51	13.69	14.35	15.47	**Al_2O_3**
5.28	4.26	4.97	4.83	**FeO***
0.06	0.11	0.08	0.06	**MnO**
0.64	0.50	0.77	0.62	**MgO**
2.50	2.00	3.20	3.66	**CaO**
5.03	4.08	4.41	4.30	**Na_2O**
2.42	3.07	2.93	2.92	**K_2O**
0.29	0.24	0.28	0.21	**P_2O_5**
	0.02		0.02	**NiO**
0.01		0.01	0.02	**SO_3**
96.17	95.34	98.53	98.33	**TOT**
				H_2O (*wt.%*) nSIMS
				CO2 (*µg/g*) nSIMS
				S (µg/g) nSIMS
				Cl (µg/g) nSIMS
				F (µg/g) nSIMS
30		41	81	**S (µg/g) EMPA**
				Cl (µg/g) EMPA
				F (µg/g) EMPA
		1029	1026	**Olivine-L °T (°C)**
				Hygrometer H_2O (wt. %) *L
				Hygrometer H_2O (wt. %) *L2
				P(kbar)
				°T(°C)
				$KD_{(Ab\text{-}An)}$

NExtra_CC1l1c7v3 Olivine-rimivine-rim Cono Cancion	NExtra_CC1l1c7v4 Olivine-rimivine-rim Cono Cancion	NExtra_CC1l1c7v5 Olivine-rimivine-rim Cono Cancion	NExtra_CC1l1c7v6 Olivine-rimivine-rim Cono Cancion	PR1_cc1f6c1v1 Plagioclase-rim Cono Cancion	PR1_cc1f6c1v2 Plagioclase-rim Cono Cancion
66.16	53.74	66.39	66.02	66.25	64.99
1.09	0.10	1.03	1.15	1.18	1.19
14.52	27.27	15.17	13.79	13.35	14.14
4.65	0.98	4.19	4.30	6.26	5.64
0.05	0.05	0.08	0.06	0.12	0.06
0.59	0.18	0.60	0.80	0.94	0.72
3.30	11.07	3.63	2.46	2.86	3.11
4.39	4.58	4.53	3.83	4.49	4.00
2.82	0.32	2.34	4.18	2.94	3.36
0.21	0.04	0.28	0.25	0.30	0.31
0.12	0.02			0.03	0.09
0.00				0.03	0.03
97.92	98.34	98.24	96.84	98.75	97.64
		0.61			
		80			
		6			
		1259			
		508			
10				102	102
1026	1018	1026	1030		
				0.43	0.92
				2.51	3.43
				14.9	16.1
				1045	1030
				0.24	0.26

Inclusion Phenocryst	PR1_cc1f6c1v3	PR1_cc1f6c1v4	PR1_cc1f6c1v5	
Groundmass spot	Plagioclase-rim	Plagioclase-rim	Plagioclase-rim	
Stratigraphy	Cono Cancion	Cono Cancion	Cono Cancion	Tolhuaca Fissural
SiO_2, *wt.%*	66.49	66.12	67.04	
TiO_2	1.19	1.19	1.17	
Al_2O_3	13.58	13.45	13.98	
FeO*	5.49	5.85	5.18	
MnO	0.06	0.11	0.14	
MgO	0.78	0.80	0.78	
CaO	2.85	2.86	2.75	
Na_2O	4.88	4.50	4.87	
K_2O	2.59	2.81	2.97	
P_2O_5	0.24	0.35	0.32	
NiO	0.08	0.11	0.02	
SO_3	0.03	0.02		
TOT	98.25	98.16	99.22	
H_2O (*wt.%*) nSIMS				
CO2 (*µg/g*) nSIMS				
S (µg/g) nSIMS				
Cl (µg/g) nSIMS				
F (µg/g) nSIMS				
S (µg/g) EMPA	122	92		
Cl (µg/g) EMPA				
F (µg/g) EMPA				
Olivine-L °T (°C)				
Hygrometer H_2O (wt. %) *L	0.43	0.50	0.61	
Hygrometer H_2O (wt. %) *L2	2.75	2.74	3.00	
P(kbar)	15.5	15.1	16.6	
°T(°C)	1047	1042	1038	
$KD_{(Ab\text{-}An)}$	0.24	0.24	0.25	

NExtra_to1a104v1	NExtra_to1a104v2	**Inclusion Phenocryst**	NExtra_to1a104v3	NExtra_to1a104v4
Augite-rim	Augite-rim	**Groundmass spot**	Augite-rim	Augite-rim
Tolhuaca Fissural	Tolhuaca Fissural	**Stratigraphy**	Tolhuaca Fissural	Tolhuaca Fissural
56.46	55.80	**SiO_2,** *wt.%*	55.52	55.79
1.85	1.78	**TiO_2**	1.90	1.99
12.81	13.18	**Al_2O_3**	12.68	13.93
11.75	11.68	**FeO***	11.82	10.70
0.11	0.15	**MnO**	0.15	0.17
3.31	3.84	**MgO**	3.50	3.09
7.21	7.27	**CaO**	7.18	7.52
2.95	3.25	**Na_2O**	3.15	3.26
1.28	1.26	**K_2O**	1.36	1.22
0.42	0.39	**P_2O_5**	0.45	0.48
0.01		**NiO**	0.04	
0.02		**SO_3**	0.05	
98.17	98.60	**TOT**	97.79	98.15
		H_2O (*wt.%*) nSIMS	0.14	
		CO2 (*µg/g*) nSIMS	0	
		S (µg/g) nSIMS	9	
		Cl (µg/g) nSIMS	385	
		F (µg/g) nSIMS	392	
100		**S (µg/g) EMPA**	199	
		Cl (µg/g) EMPA		
		F (µg/g) EMPA		
		Olivine-L °T (°C)		
		Hygrometer H_2O (wt. %) *L		
		Hygrometer H_2O (wt. %) *L2		
		P(kbar)		
		°T(°C)		
		$KD_{(Ab-An)}$		

NExtra_to1a104v5	NExtra_to1a104v6	PR1_to1af7c6v1	PR1_to1af7c6v2	**Inclusion Phenocryst**
Augite-rim	Augite-rim	Augite-rim	Augite-rim	**Groundmass spot**
Tolhuaca Fissural	Tolhuaca Fissural	Tolhuaca Fissural	Tolhuaca Fissural	**Stratigraphy**
55.83	54.45	55.28	56.32	**SiO_2,** *wt.%*
1.81	1.86	1.77	1.84	**TiO_2**
13.09	12.42	13.32	13.32	**Al_2O_3**
11.83	12.27	11.77	11.59	**FeO***
0.18	0.17	0.13	0.11	**MnO**
3.30	3.33	3.66	3.72	**MgO**
7.04	7.09	7.02	6.78	**CaO**
3.06	3.02	3.40	3.30	**Na_2O**
1.40	1.24	1.44	1.19	**K_2O**
0.33	0.46	0.50	0.47	**P_2O_5**
0.07	0.08	0.08	0.02	**NiO**
0.02	0.01	0.00	0.00	**SO_3**
97.96	96.39	98.36	98.65	**TOT**
				H_2O (*wt.%*) nSIMS
				CO2 (*µg/g*) nSIMS
				S (µg/g) nSIMS
				Cl (µg/g) nSIMS
				F (µg/g) nSIMS
100	20	10	10	**S (µg/g) EMPA**
				Cl (µg/g) EMPA
				F (µg/g) EMPA
				Olivine-L °T (°C)
				Hygrometer H_2O (wt. %) *L
				Hygrometer H_2O (wt. %) *L2
				P(kbar)
				°T(°C)
				$KD_{(Ab\text{-}An)}$

PR1_to1af7c6v3	PR1_to1af7c6v4	PR1_to1af7c6v5	PR2_to1a12v5Xv1	PR2_to1a12v5Xv2
Augite-rim	Augite-rim	Augite-rim	Augite-rim	Augite-rim
Tolhuaca Fissural	Tolhuaca Fissural	Tolhuaca Fissural	Tolhuaca Fissural	Tolhuaca Fissural
55.47	57.32	57.69	56.35	56.37
1.78	1.98	1.87	1.92	1.71
13.67	12.82	12.75	13.32	12.47
10.69	12.11	11.77	11.49	11.55
0.14	0.19	0.15	0.14	0.18
3.43	3.71	4.28	3.52	5.01
6.76	7.17	7.26	7.19	7.17
4.25	3.31	3.20	3.03	3.53
1.35	1.25	1.22	1.37	1.24
0.42	0.46	0.44	0.42	0.47
		0.10		0.07
0.03		0.03		0.01
98.00	100.32	100.76	98.74	99.78

130	120	30

PR2_to1a12v5Xv3	**Inclusion Phenocryst**	PR2_to1a12v5Xv4	PR2_to1a12v5Xv5	PR2_to1a12v5Xv6
Augite-rim	**Groundmass spot**	Augite-rim	Augite-rim	Augite-rim
Tolhuaca Fissural	**Stratigraphy**	Tolhuaca Fissural	Tolhuaca Fissural	Tolhuaca Fissural
55.90	**SiO_2,** *wt.%*	56.13	56.13	55.89
1.46	**TiO_2**	1.84	2.03	1.82
10.58	**Al_2O_3**	12.53	13.31	13.68
12.08	**FeO***	12.29	12.17	11.29
0.16	**MnO**	0.22	0.19	0.18
7.47	**MgO**	4.56	3.53	3.47
8.02	**CaO**	7.18	7.10	7.41
2.74	**Na_2O**	3.11	2.90	3.10
0.95	**K_2O**	1.34	1.17	1.14
0.25	**P_2O_5**	0.42	0.44	0.40
0.02	**NiO**	0.06		0.05
0.03	**SO_3**	0.03		0.05
99.66	**TOT**	99.72	98.98	98.48
	H_2O (*wt.%*) nSIMS			
	CO2 (*µg/g*) nSIMS			
	S (µg/g) nSIMS			
	Cl (µg/g) nSIMS			
	F (µg/g) nSIMS			
128	**S (µg/g) EMPA**	128		185
	Cl (µg/g) EMPA			
	F (µg/g) EMPA			
	Olivine-L °T (°C)			
	Hygrometer H_2O (wt. %) *L			
	Hygrometer H_2O (wt. %) *L2			
	P(kbar)			
	°T(°C)			
	$KD_{(Ab\text{-}An)}$			

PR2_to1a49Xr_v	PR2_to1a49Xr_v2	PR2_to1a49Xr_v3	**Inclusion Phenocryst**	PR2_to1a49Xr_v4
Olivine-rim	Olivine-rim	Olivine-rim	**Groundmass spot**	Olivine-rim
Tolhuaca Fissural	Tolhuaca Fissural	Tolhuaca Fissural	**Stratigraphy**	Tolhuaca Fissural
54.13	55.09	54.65	**SiO_2,** *wt.%*	53.66
0.16	0.02	0.22	**TiO_2**	0.39
25.69	26.64	26.54	**Al_2O_3**	18.43
1.62	1.19	1.34	**FeO***	7.94
0.03	0.01		**MnO**	0.19
0.11	0.11	0.16	**MgO**	5.59
9.44	10.48	10.15	**CaO**	8.06
4.98	4.91	5.00	**Na_2O**	3.71
0.49	0.47	0.52	**K_2O**	0.56
0.06	0.04	0.06	**P_2O_5**	0.23
0.05			**NiO**	
	0.04	0.01	**SO_3**	
96.76	99.00	98.64	**TOT**	98.76
			H_2O (*wt.%*) nSIMS	
			CO2 (*µg/g*) nSIMS	
			S (µg/g) nSIMS	
			Cl (µg/g) nSIMS	
			F (µg/g) nSIMS	
	176	49	**S (µg/g) EMPA**	
			Cl (µg/g) EMPA	
			F (µg/g) EMPA	
1016	1016	1017	**Olivine-L °T (°C)**	1126
			Hygrometer H_2O (wt. %) *L	
			Hygrometer H_2O (wt. %) *L2	
			P(kbar)	
			°T(°C)	
			$KD_{(Ab\text{-}An)}$	

PR2_to1a49Xr_v5	PR2_to1a49Xr_v6	PR1_to1af1c7Xv3	PR1_to1af1c7Xv5	PR1_to1b61_v1
Olivine-rim	Olivine-rim	Augite-rim	Augite-rim	Olivine-rim
Tolhuaca Fissural	Tolhuaca Fissural	Tolhuaca Fissural	Tolhuaca Fissural	Tolhuaca Fissural
56.20	44.71	53.58	53.44	55.78
0.12	0.34	1.84	1.71	0.10
25.18	2.87	11.70	12.30	27.58
1.20	29.33	11.23	11.23	1.32
0.00	0.45	0.13	0.21	0.01
0.18	19.76	3.21	3.16	0.13
9.63	1.48	7.63	7.59	10.69
4.87	0.60	2.21	2.20	5.03
0.83	0.18	1.27	1.24	0.47
0.00	0.25	0.35	0.36	
0.01			0.08	0.00
	0.01	0.02	0.03	0.03
98.23	99.98	93.17	93.55	101.14

58 70 129 111

1018 1411 1017

Inclusion Phenocryst	PR1_to1b61_v2	NExtra_ca02a23_mia	NExtra_ca02a23_mia2
Groundmass spot	Olivine-rim	Olivine-rim	Olivine-rim
Stratigraphy	Tolhuaca Fissural	Cono Caracol	Cono Caracol
SiO_2, *wt.%*	54.36	44.54	42.62
TiO_2	0.16	0.06	
Al_2O_3	26.15	34.49	32.93
FeO*	1.59	1.09	2.63
MnO	0.04		0.05
MgO	0.40	0.13	3.20
CaO	10.63	18.85	17.28
Na_2O	4.61	0.70	0.67
K_2O	0.48	0.02	0.05
P_2O_5			
NiO	0.03	0.06	0.04
SO_3	0.01	0.01	
TOT	98.45	99.95	99.47
H_2O (*wt.%*) nSIMS		0.00	
CO2 (*µg/g*) nSIMS		20	
S (µg/g) nSIMS		0	
Cl (µg/g) nSIMS		6	
F (µg/g) nSIMS		70	
S (µg/g) EMPA	20	50	
Cl (µg/g) EMPA			
F (µg/g) EMPA			
Olivine-L °T (°C)	1022	1017	1078
Hygrometer H_2O (wt. %) *L			
Hygrometer H_2O (wt. %) *L2			
P(kbar)			
°T(°C)			
$KD_{(Ab-An)}$			

Table 6 SIMS analyses of Tolhuaca PEC glass inclusions

Inclusion SIMS	**Volcano**	**H_2O (wt%)**	**CO_2 (µg/g)**	**S (µg/g)**	**Cl (µg/g)**
NExtra_CC1m65r	Cono Canción	1.77	-	49	4082
NExtra_CC1m65r	Cono Canción	1.54	-	39	3430
PR1_to1af1c7Xv5	Tolhuaca Fissural	0.61	80	6	1259
PR1_to1af1c7Xv5	Tolhuaca Fissural	0.61	80	6	1259
NExtra_to1a29_miac	Tolhuaca Fissural	1.40	126	471	377
NExtra_to1a29_mibr	Tolhuaca Fissural	1.48	188	497	397
NExtra_to1a32_mic	Tolhuaca Fissural	1.41	165	467	398
NExtra_to1a104v3	Tolhuaca Fissural	0.14	-	9	385
NExtra_tolb9mi	Tolhuaca Fissural	1.94	2497	143	1095
NExtra_ca02a23_mia	Cono Caracol	0.00	20	0	6
519@1	Glass Standard	0.22	590	1065	73
519@2	Glass Standard	0.23	378	1087	75
519-4-1*	Literature	0.17	165	1020	-
	STD 519-1-4	33.4	128.8	6.5	n.d.
Standard #2. GL07 D31	Glass Standard	1.51	19	1516	811
GL07 D31**	Literature	1.54	-	-	-
	STD GL07 D31	1.9	n.d.	n.d.	n.d.

*Fine and Stolper, (1986) in Hauri et al. (2002)

**Dixon and Kingsley, unpublished dat. In Hauri et al. (2002)

F (µg/g)
449
379
508
508
305
318
321
392
189
70
181
185
-
n.d.
892
-
n.d.

Table 7: Chemical and isotope compositions of noble gases in fluid inclusions of olivine

Sample ID	Period of volcanism	^{4}He mol/g	^{21}Ne mol/g	^{22}Ne mol/g	^{40}Ar mol/g
Villa_p2015lmic*	3 March 2015 paroxysmal eruption	1.27E-13	-	-	6.15E-12
CC1	Tolhuaca-ConoCancion	3.52E-14	6.91E-18	2.41E-16	1.38E-12
TO1A	Tolhuaca-Cordon Fissural	4.93E-15	7.62E-18	2.65E-16	1.87E-12
TO1B	Tolhuaca-Cordon Fissural	1.94E-15	4.01E-18	1.38E-16	1.01E-12
NV-18	Tolhuaca-Cordon Fissural	1.67E-14	2.63E-18	9.21E-17	3.49E-13
CA02A	Tolhuaca-Cono Caracol	5.57E-15	9.73E-18	3.40E-16	1.48E-12

^{36}Ar	R/Ra	$^{4}He/^{20}Ne$	Rc/Ra	Err.	$^{40}Ar/^{36}Ar$	Err.	$^{40}Ar^{*}$	$^{4}He/^{40}Ar^{*}$	$CO_2/^{3}He$	Mg#	err
mol/g				+/-		%	mol/g			%	%
2.038E-14	6.43	50.8	6.46	0.12	301.6	0.1	-	1.02	1.30.E-11	77.00	-
4.34E-15	6.27	14.5	6.40	0.38	320.4	0.06	1.38E-10	0.37	1.37.E+09	72.58	-
6.33E-15	6.90	1.9	8.16	0.63	299.0	0.05	2.01E-10	1.52	1.41.E+09	80.79	1.65
3.42E-15	5.91	1.4	7.41	0.84	299.1	0.06	1.09E-10	0.94	1.86.E+10	81.04	1.47
1.13E-15	6.18	18.7	6.28	0.30	312.0	0.10	3.59E-11	1.11	2.64.E+08	80.79	1.65
5.00E-15	5.44	1.7	6.56	0.58	299.9	0.05	6.65E-15	0.84	5.12E+08	80.417	1.57

Declaration of interests

☒The authors declare that they have no known competing financial interests or personal relationships that could have appeared to influence the work reported in this paper.

☐The authors declare the following financial interests/personal relationships which may be considered as potential competing interests:

Supplementary Material Table S2

Supplementary Material Table S3

Supplementary Material Table S4